JGR Atmospheres

RESEARCH ARTICLE
10.1029/2024JD040748

West African Monsoon Dynamics and Its Control on the Stable Oxygen Isotopic Composition of Precipitation in the Late Cenozoic

Daniel Boateng[1], Jeffrey N. A. Aryee[2], Michael Baidu[3], Frank Arthur[4], and Sebastian G. Mutz[5]

[1]Department of Geosciences, University of Tübingen, Tübingen, Germany, [2]Department of Meteorology and Climate Science, Kwame Nkrumah University of Science and Technology, Kumasi, Ghana, [3]Institute for Climate and Atmospheric Science, School of Earth and Environment, University of Leeds, Leeds, UK, [4]Department of Natural Sciences and Environmental Health, University of South-Eastern Norway, Bø i Telemark, Norway, [5]School of Geographical and Earth Sciences, University of Glasgow, Glasgow, UK

Key Points:

- We simulate the Late Cenozoic evolution of the West African Monsoon and the isotopic composition of rainwater
- Using a high-resolution model setup and realistic vegetation cover increases the intensity of the West African Monsoon in the Mid-Holocene due to the pronounced meridional temperature gradient
- The relationship between precipitation and the simulated isotopes is non-stationary in time, which complicates proxy climate reconstructions

Supporting Information:

Supporting Information may be found in the online version of this article.

Correspondence to:

D. Boateng,
daniel.boateng@uni-tuebingen.de

Citation:

Boateng, D., Aryee, J. N. A., Baidu, M., Arthur, F., & Mutz, S. G. (2024). West African Monsoon dynamics and its control on the stable oxygen isotopic composition of precipitation in the Late Cenozoic. *Journal of Geophysical Research: Atmospheres*, *129*, e2024JD040748. https://doi.org/10.1029/2024JD040748

Received 5 JAN 2024
Accepted 5 MAY 2024

Author Contributions:

Conceptualization: Daniel Boateng
Formal analysis: Daniel Boateng
Funding acquisition: Sebastian G. Mutz
Investigation: Daniel Boateng
Methodology: Daniel Boateng, Jeffrey N. A. Aryee, Michael Baidu, Frank Arthur
Software: Daniel Boateng
Supervision: Sebastian G. Mutz
Validation: Daniel Boateng, Jeffrey N. A. Aryee, Michael Baidu
Visualization: Daniel Boateng
Writing – original draft: Daniel Boateng

Abstract This study presents an overview of the Late Cenozoic evolution of the West African Monsoon (WAM), and the associated changes in atmospheric dynamics and oxygen isotopic composition of precipitation ($\delta^{18}O_p$). This evolution is established by using the high-resolution isotope-enabled GCM ECHAM5-wiso to simulate the climatic responses to paleoenvironmental changes during the Mid-Holocene (MH), Last Glacial Maximum (LGM), and Mid-Pliocene (MP). The simulated responses are compared to a set of GCM outputs from Paleoclimate Model Intercomparison Project Phase 4 (PMIP4) to assess the added value of a high resolution and model consistency across different time periods. Results show WAM magnitudes and pattern changes that are consistent with PMIP4 models and proxy reconstructions. ECHAM5-wiso estimates the highest WAM intensification in the MH, with a precipitation increase of up to 150 mm/month reaching 25°N during the monsoon season. The WAM intensification in the MP estimated by ECHAM5-wiso (up to 80 mm/month) aligns with the mid-range of the PMIP4 estimates, while the LGM dryness magnitude matches most of the models. Despite an enhanced hydrological cycle in MP, MH simulations indicate a ∼50% precipitation increase and a greater northward extent of WAM than the MP simulations. Strengthened conditions of the WAM in the MH and MP result from a pronounced meridional temperature gradient driving low-level westerly, Sahel-Sahara vegetation expansion, and a northward shift of the Africa Easterly Jet. The simulated $\delta^{18}O_p$ values patterns and their relationship with temperature and precipitation are non-stationarity over time, emphasizing the implications of assuming stationarity in proxy reconstruction transfer functions.

Plain Language Summary We use a global climate model to simulate how the West African Monsoon and related climate elements changed over the Late Cenozoic (from ca. 3 million years ago to now). We use a single, high-resolution model to calculate these changes for the Mid-Holocene, Last Glacial Maximum and Mid-Pliocene time periods. We then compare our results to already existing simulations to find out if there are any benefits to using a single, high-resolution model set-up. Overall, our simulations are similar to previous simulations and other climate reconstructions. However, our results also yield two important new findings: (a) our simulations reproduce some aspects of the monsoon better than previous simulations; (b) the chemical composition of rainwater, which is used by geologists to reconstruct climate, is impacted by more factors than previously assumed. This makes it more challenging to create reliable reconstructions of climate from geological records of rainwater composition.

1. Introduction

Understanding the complex climate dynamics and variability over West Africa has been a pertinent concern due to its strong environmental and socio-economic impacts. This is especially important since most West African countries rely on a rainfed agriculture economy (Sultan et al., 2005). Most importantly, the long-lasting multi-decadal wet and dry periods during the 20th century emphasize the need to understand the long-term and future variability of the West African Monsoon (WAM) system. This requires knowledge about the response of the WAM dynamics to changes in internal feedbacks and external forcings, such as orbital parameters, atmospheric greenhouse gases, and vegetation distribution. Considering past climate change outside the recent observational period can provide valuable insights into that. More specifically, time periods with atmospheric CO_2

Writing – review & editing: Jeffrey N. A. Aryee, Michael Baidu, Frank Arthur, Sebastian G. Mutz

concentrations (pCO_2) and paleogeography similar to the present day can serve as analog for a possible future climate in which all forcings have had their full effect. This would require looking back 3 million years in Earth's history (Burke et al., 2018). Therefore, this study focuses on a model-based exploration of the evolution of the WAM from the Mid-Pliocene (MP: ∼3 Ma) to the present-day, considering the Last Glacial Maximum (LGM: ∼21 ka), and Mid-Holocene (MH: ∼6 ka) as important intermediate time steps.

Due to the complicated dynamics and teleconnections of the WAM, state-of-art General Circulation Models (GCMs) still fall short in accurately reproducing its past variability and providing consistent future projections (Biasutti, 2013; Pausata et al., 2016; Tierney et al., 2017). Improving the representation of the WAM system in climate models requires knowledge about its sensitivity to various global and regional paleoenvironment forcings and feedbacks. This knowledge can help identify the elements that need improvement in GCMs to ensure more reliable predictions of the WAM in the future. For instance, the response of the WAM dynamics to orbitally driven seasonal and latitudinal distribution of incoming solar radiation can be evaluated under MH conditions (Joussaume et al., 1999; Kutzbach & Liu, 1997). The LGM provides an opportunity to study the response of the WAM to the most recent global cold extreme, characterized by extensive ice sheet coverage and low pCO_2 concentrations (e.g., Bereiter et al., 2015). The long-term sensitivity of the WAM to pCO_2 concentrations similar to the present, along with a less arid Sahara and a globally enhanced hydrological cycle, can also be assessed under MP paleoenvironment conditions (Corvec & Fletcher, 2017; Dowsett et al., 2010; Haywood et al., 2020; Salzmann et al., 2008).

Despite the challenges in replicating the entirety of past climate changes with GCMs under appropriate paleoenvironmental conditions (Braconnot et al., 2012; Harrison et al., 2015), comparing the simulated responses from different climate models would shed more light on the inadequate representation of feedbacks and model biases that can be improved for future climate predictions (e.g., Zheng & Braconnot, 2013). Furthermore, such intermodel comparison across multiple past climates would help determine if the systematic model biases affect the overall strength of the responses and feedbacks in the different climates and help evaluate if such biases are GCM-specific or exist independently of the GCM that is used.

Numerous modeling studies have simulated the precipitation changes associated with the WAM in response to multiple forcings and climate states during the Late Cenozoic (e.g., Berntell et al., 2021; Weldeab et al., 2011; Zheng & Braconnot, 2013). However, the differences between the simulations, such as spatial resolution, boundary conditions, and the complexity of the GCM, make it difficult to identify the predominant atmospheric dynamics behind the WAM precipitation changes. For instance, model-dependent uncertainties of the individual GCMs that simulated these climates in previous studies may not fully capture certain components of the WAM system, which can amplify the systematic biases related to the sensitivity to various forcings or external perturbations across different climates. Moreover, GCMs with varied spatial resolutions and parameterizations of clouds, atmospheric dynamics, hydrological cycles, and atmosphere-land surface interactions would simulate distinct responses of the WAM to different forcings, leading to inconsistent patterns of WAM dynamics. Aside from these, only a few studies have comprehensively delved into atmospheric dynamics and teleconnections behind the changes in precipitation patterns and magnitudes under different paleoenvironmental conditions throughout the Late Cenozoic (e.g., Bosmans et al., 2012; Gaetani et al., 2017; Patricola & Cook, 2007; Su & Neelin, 2005). Furthermore, previous studies have highlighted that monsoons and related circulations, such as the Inter Tropical Convergence Zone (ITCZ), are better resolved at higher resolutions, including improved topographical representation and model parameterization (Bosmans et al., 2012; Gao et al., 2006; Jungandreas et al., 2021). This study addresses the points above by providing details about the WAM atmospheric dynamics across these past climates using a consistent modeling framework with a high-resolution isotope-enabled GCM.

Geological archives can record information about various paleoenvironmental changes in the climate system over time. They can therefore be used for model-data comparisons and as a benchmark for climate models (Braconnot et al., 2012; Harris et al., 2014; Harrison et al., 2015). However, the scarcity of palaeohydrological records over Africa and the spatial resolution of climate models preclude the robust model-data comparison necessary for improving climate models (e.g., Salzmann et al., 2008, 2013). Several problems for data-model persist in this region. For instance, proxy-based reconstructions using pollen, past lake levels, leaf wax isotopes, and other records have suggested significantly wetter conditions across the Sahel and Sahara during the MH (Ait Brahim et al., 2023; Bartlein et al., 2011; Tierney et al., 2017). However, most climate models struggle to replicate the extent and magnitude of precipitation changes indicated by these proxy records despite accounting for factors like

increased insolation, altered land surface condition (e.g., vegetation, lakes, orography, soil moisture), reduced dust emissions, atmospheric-ocean interactions, and atmospheric dynamics (deMenocal et al., 2000; Harrison et al., 2014; Hopcroft & Valdes, 2019, 2022; Pausata et al., 2016; Tierney et al., 2017).

While proxy records point to varying increases in precipitation levels over North Africa's higher latitudes, climate models estimate a more moderate WAM intensification, underestimating both the northward extent and magnitude of precipitation increase suggested by the proxies. If the proxy data is a well-collected, representative sample, there are two possible model-related reasons for this mismatch: (a) The climate models simply do not capture the atmospheric processes in the region well enough to accurately model said hydroclimate changes. (b) Proxy system models, which allow the conversion of the proxy signal to a paleoclimate signal, are flawed. Proxy system models rely on calibrations based on modern-day observations, such as the spatial correlation between water isotopes and precipitation. These are used to establish a transfer function that allows a proxy-to-climate signal conversion. This signal transformation assumes that the transfer functions are stationary in time, that is, that modern correlations are equally valid for past climates. This study uses an isotope-enabled GCM to decipher atmospheric dynamics driving WAM changes and to explore their impacts on water isotopologues under various past global changes. This allows for the testing of this assumption of the stationarity of the transfer function. Furthermore, such an analysis facilitates a direct model-isotope proxy comparison and contributes to understanding the general causal mechanisms behind the variability in different proxy materials (Bühler et al., 2022; Phipps et al., 2013; Risi et al., 2012; Werner et al., 2000).

This study provides the first overview of the changes of the WAM and its associated atmospheric dynamics in response to multiple forcings and feedbacks during the Late Cenozoic, using the high-resolution isotope-enabled GCM ECHAM5-wiso. More specifically, the study addresses the following specific objectives: (a) systematically simulating the responses of the WAM patterns and magnitude to the various paleoenvironment conditions, including changes in vegetation, orbital forcings, ice sheet extent, and atmospheric CO_2 concentrations; (b) investigating the atmospheric dynamics driving the simulated WAM changes, such as moisture transport (e.g., low-level southwesterlies), Africa Easterly Jet (AEJ), Tropical Easterly Jet (TEJ), Sahara Heat Low (SHL) and surface heat fluxes; and (c) exploring the simulated $\delta^{18}O_p$ values and how they are influenced by near-surface temperature and precipitation in response to the different boundary conditions. We further compare the simulated changes of the WAM to some of the state-of-the-art models that participated in the Paleoclimate Model Intercomparison Project (PMIP4) Phase 4 to evaluate the added values of using a consistent, high-resolution modeling framework to understand the complex climate system over West Africa and improve its representation in Earth system models.

2. Background

2.1. On the Intensification and Northward Extent of the West African Monsoon During the Mid-Holocene

During the early-to-middle Holocene, spanning from 11,000 to 5,000 years before the present, the arid landscapes of the Sahel and Sahara regions transformed into shrubs, grasslands, and water bodies like rivers and lakes (Armitage et al., 2015; Claussen et al., 1999; deMenocal et al., 2000; Holmes, 2008; Kohfeld & Harrison, 2000). The development of this "Green Sahara" was attributed to changes in the insolation cycle, which intensified the equator-to-pole gradient and land-sea thermal contrasts and ultimately lead to an increase in rainfall across the Sahel-Sahra. The associated pressure gradient facilitated the moisture transport from the equatorial Atlantic into the continent. Overall, the changes in the orbital cycles and expansion of vegetation across the Sahel-Sahara caused the strengthening of the WAM and its northward extent (Gaetani et al., 2017; Hopcroft & Valdes, 2022; Patricola & Cook, 2007). This WAM intensification and northward migration have been reflected in many proxy systems such as paleo-lake levels (Hoelzmann et al., 1998; Prentice et al., 2000), leaf wax, and aeolian deposits in sedimentary cores from the Eastern Atlantic (deMenocal et al., 2000; Tierney et al., 2017) and archeological findings that indicate human habitation (Cremaschi & Di Lernia, 1999; Dunne et al., 2012; Gabriel, 1987; Hoelzmann et al., 2001; Manning & Timpson, 2014; Sereno et al., 2008). However, state-of-art climate models still struggle to replicate the level of intensification and the northward reach as suggested by the different proxies, even when appropriate boundary conditions are prescribed (deMenocal et al., 2000; Harrison et al., 2014; Hopcroft & Valdes, 2019; Kutzbach & Liu, 1997; Pausata et al., 2016; Tierney et al., 2017). For instance, MH simulations in PMIP3-CMIP5 experiments estimate a precipitation increase of ~400 mm/year over West Africa, with a northward shift that is underestimated by 20°N when compared to proxy reconstructions

(Perez-Sanz et al., 2014). Thompson et al. (2021) utilized a water isotope-enabled Earth system model (iCESM1) that exhibited enhanced MH precipitation compared to PI conditions, and a northernmost WAM shift of approximately 24°N, which aligns with reconstructions from pollen and dust records (23–28°N). Most of these models, however, lack vegetation feedback or appropriate prescribed MH vegetation reconstruction, which is crucial for sustaining the WAM's northward extension through vegetation-precipitation feedback (Otto-Bliesner et al., 2017; Pausata et al., 2016; Tierney et al., 2017). Rachmayani et al. (2015) demonstrated that using dynamic vegetation-coupled GCMs enhances the orbitally-induced precipitation increase by 20% over West Africa compared to fixed vegetation GCMs.

Recent studies have also highlighted that accounting for dust feedbacks related to the Green Sahara during the MH can further intensify and expand the WAM, aligning it more with proxy reconstructions (e.g., Egerer et al., 2018; Hopcroft & Valdes, 2019; Pausata et al., 2016; Thompson et al., 2019). These findings indicate that the discrepancies between the model and proxy reconstructions are due to the inadequate representation of certain atmospheric physics, such as inaccurate cloud representation, energy fluxes, subgrid-scale convection, and surface conditions in the GCMs. Moreover, the coarse spatial resolution of GCMs fails to capture meso-to-local-scale processes like mesoscale convective systems (e.g., Baidu et al., 2022; Crook et al., 2019; Marsham et al., 2013), potentially contributing to further biases. Thus, understanding the mechanics and dynamics underlying vegetation feedback and natural variability in insolation cycles driving the WAM's northward migration during the MH is crucial for evaluating GCM performance in future projections. While these forcing mechanisms are not linked to anthropogenic emissions, evaluating and improving the GCMs' representation of climate system dynamics and feedbacks is vital for future climate change projections.

2.2. Large-Scale Feature of the Last Glacial Maximum and Its Influence on the West African Monsoon

The LGM (~21,000 years BP) is a time period that is suitable for assessing the capabilities of state-of-the-art models due to its starkly different conditions from the present, such as lower atmospheric CO_2 levels (~185 ppm) and eustatic sea levels (~115–130 m below present) (Lambeck et al., 2014; Peltier & Fairbanks, 2006). The extensive continental ice sheets led to significant perturbations in atmospheric radiative forcing and circulation patterns, contributing to alterations in precipitation and temperature that were generally drier and colder than pre-industrial conditions (Clark et al., 2009; D'Agostino et al., 2019, 2020). Since the LGM, the Earth's global mean temperature has risen by approximately 4–6°C (Annan & Hargreaves, 2013, 2015; Friedrich et al., 2016), which is of the same order of magnitude increase projected under moderate to high emission scenarios for near-future climate change. Due to this similarity in global forcing and temperature response from the LGM to the present, and the present to the near future, the LGM is a relevant period to examine (e.g., Brady et al., 2013; Yoshimori et al., 2009). The LGM represents a test bed to conduct the out-of-sample evaluation of the strength and stability of key climate system feedbacks and large-scale responses to regional hydroclimate changes. Furthermore, the interactions between temperature-driven and circulation-driven regional precipitation patterns in response to LGM conditions would help evaluate the ability of climate models to project precipitation under future scenarios, where both thermodynamic and dynamic phenomena contribute to changes in the magnitude and seasonality of precipitation patterns (e.g., Boos, 2012; Lora, 2018; Scheff & Frierson, 2012).

Prior studies have indicated a high sensitivity of Africa's climate to rapid recurring ice sheet instabilities during the last glacial period (Adegbie et al., 2003; Stager et al., 2002, 2011; Weldeab et al., 2011). For example, the cold air temperatures over Greenland (Dansgaard-Oeschger stadials) and the influx of meltwater into the North Atlantic during Heinrich events correlated with the rapid decline in precipitation across much of Africa (Blunier & Brook, 2001; Dansgaard et al., 1993; McManus et al., 2004). Previous modeling studies of PMIP phases 1 to four indicated weakened atmospheric circulation and associated decreased precipitation over West Africa (Kageyama et al., 2021). However, a good understanding of the dynamics leading to the dryness across the WAM region is still lacking. The comparison of the atmospheric dynamics changes of the LGM to other warmer climates will help reveal the predominant atmospheric processes relevant to the variability of the WAM and help improve their representation in climate models for future climate projections.

Pollen-based reconstructions across the WAM and nearby offshore regions generally depict colder and drier conditions than the present (Bartlein et al., 2011). Although fully coupled atmosphere-ocean models can reasonably reproduce large-scale features of the LGM, several challenges remain with regard to the reconstruction of LGM topography and the assessment of inter-model biases for various climate feedbacks (Kageyama

et al., 2021; Werner et al., 2018). Additionally, the spatial resolution of simulations has been identified as a crucial factor for the inter-model variabilities in LGM simulations, primarily due to the representation of ice sheet topography (Kim et al., 2008; Shi et al., 2020). Overall, the complexity and diverse paleoenvironment of LGM conditions offers the opportunity to decipher the relative contributions of individual climate factors that influence precipitation changes across West Africa. The response of reginal $\delta^{18}O$ in precipitation distribution in the LGM would contribute to the interpretation of proxy signals to ensure robust model-data comparison that can be used to constrain the sensitivity of climate models.

2.3. Changes of the WAM in the Mid-Pliocene

The MP (~3 Ma) is an important warm period for understanding the atmospheric dynamics of near-future climate change, because the Earth's geography was similar to the present and pCO_2 approached present-day values (~400 ppm) (Badger et al., 2013; Bartoli et al., 2011; Dowsett et al., 2016; Haywood et al., 2020; Salzmann et al., 2013; de la Vega et al., 2020). Additionally, the MP provides useful insights into climate feedbacks through the impact of the carbon cycle on geological times and is often considered an analog for a near-future climate (Burke et al., 2018; Jiang et al., 2005). Climate models that participated in the PlioMIP (Pliocene Modeling Intercomparison Project) phases 1 and 2 indicate an increase of 1.4–4.7°C in global mean near-surface anomalies above the pre-industrial levels, along with an enhanced hydrological cycle and strengthened global monsoons (Haywood et al., 2013, 2020; Zhang et al., 2016).

Proxy reconstructions suggest warm and humid conditions, and fewer deserts during the MP. Boreal forests and grasslands expanded into high northern latitude regions that are currently covered by tundra (Salzmann et al., 2008). Dust records along the coast of West Africa indicate a strengthened WAM and wetter conditions over the Sahara (Kuechler et al., 2018; Salzmann et al., 2008). Palynological records also suggest an expansion of vegetation over the WAM region, with high tree cover density and widespread woodland and savanna over the Sahara (Bonnefille, 2010; Salzmann et al., 2008).

Although previous modeling studies indicated that high-latitude warming could lead to a decreased meridional temperature gradient and a weakened tropical circulation, the warming experienced in the Sahara region, along with the corresponding Sahara heat low, actually caused an increased influx of moisture from the tropical Atlantic Ocean, strengthening WAM (Corvec & Fletcher, 2017; Haywood et al., 2020). More specifically, the PlioMIP2 models estimate an increase in precipitation anomalies in the range of 60–120 mm/month (Berntell et al., 2021), compared to a lesser increase of 30–60 mm/month from the PlioMIP1 (R. Zhang et al., 2016). Even though similar magnitude of changes are predicted for the future, models are still limited in capturing rainfall variability over West Africa, and future projections of it are referenced with less confidence (Biasutti, 2013; Cook, 2008; Roehrig et al., 2013). Further work and model development is needed to understand climate feedback over West Africa under high atmospheric CO_2 conditions.

2.4. Stable Oxygen Isotopic Signal as Proxy for Reconstructing the West African Monsoon

Stable water isotopes serve as integrated tracers for diverse climate processes, and reflect changes in the water cycle (Craig & Gordon, 1965; Dansgaard et al., 1993). Consequently, they have been extensively used to investigate historical climate changes and characterize the current hydrological cycle. Reconstructions of the water cycle from proxy materials typically rely on modern calibrations. The modern spatial correlation between water isotopes and climate variables, such as precipitation amount or surface temperature, is used as a transfer function for reconstructing past climatic variations from proxies. However, these paleoclimate reconstructions from isotopic archives are compromised by changes in the transfer functions due to various non-linear climatic processes influencing the spatiotemporal variability of water isotopes, such as monsoon dynamics, evaporative recycling, moisture transport pathways, source variation, vapor mixing, and precipitation dynamics (Bony et al., 2008; Risi et al., 2008, 2013). For example, the oxygen isotopic composition of precipitation ($\delta^{18}O_p$) reconstructed from calcite in speleothems from (sub)tropical regions is used to reconstruct past monsoon changes (e.g., Wang et al., 2001). However, the relationship between the cave $\delta^{18}O$ record and monsoon dynamics is complex and changes across different timescales (e.g., East Asia summer monsoon intensity controls the past cave $\delta^{18}O$ in orbital timescales (Cheng et al., 2016) while summer precipitation amount is suggested to reflect the cave $\delta^{18}O$ in centennial-decadal timescales (Tan et al., 2009, 2018; H. Zhang et al., 2019)). Hence, GCMs with explicit diagnostics of stable water isotopes can contribute to understanding their controlling mechanisms under different

climatic conditions to ensure accurate paleoclimate reconstructions. Additionally, modeling the spatial representation of water isotopes in response to distinct past climate states aids in identifying potential non-stationarities in their relationships with climate elements like monsoon characteristics or precipitation amounts. While previous studies have employed water isotopes to understand present precipitation seasonality in West Africa (e.g., Risi et al., 2010) and even during the MH (Shi et al., 2023; Thompson et al., 2021), none have explored $\delta^{18}O_p$ changes in response to Late Cenozoic paleoenvironmental conditions or assessed how water isotopes correspond to the spatial variability of precipitation and temperature during the WAM season.

3. Data and Methods

3.1. ECHAM5-wiso General Circulation Model

Global climate changes in response to late Cenozoic paleoenvironmental conditions (i.e., PI, MH, LGM, and MP) and present-day (PD) conditions were simulated using the isotope-tracking climate model ECHAM5-wiso. ECHAM5 is the fifth generation of the well-established atmospheric general circulation model developed by the Max Planck Institute for Meteorology (Roeckner et al., 2003). It is based on the spectral forecast model of the European Center of Medium Range Weather Forecast (ECMWF) (Simmons et al., 1989) and represents the climate system with prognostic equations and parameterizations. Compared to its previous version, the fifth version has improved the representation of land surfaces, shortwave radiation, cumulus convection, and other factors relevant to atmospheric dynamics across the monsoon region. Specifically, the model employs an implicit scheme for the coupling of land surfaces and the atmosphere, enabling synchronous calculation of surface fluxes due to unconditional stability (Roeckner et al., 2003). It also employs land surface parameters that effectively portray the global distribution of major ecosystem types (Hagemann, 2002). Furthermore, the model simulates clouds using prognostic equations for all water phases (vapor, liquid, and solid), bulk microphysics, and statistical cloud cover parameterization (Lohmann & Roeckner, 1996; Tompkins, 2002). The version employed in this study has been expanded to include isotope tracking capabilities, enabling the simulation of the water's isotopic composition as part of the hydrological cycle (Werner et al., 2011). The incorporated water isotopologues (i.e., $H_2{}^{16}O$, $H_2{}^{18}O$, and HDO) function as independent tracers that undergo both kinetic and equilibrium fractionation during phase transitions in the atmosphere. Comparing the simulated annual mean $\delta^{18}O_p$ values with observed GNIP stations for present-day (1979–2014) indicates very similar patterns globally and a linear fit with coefficient of determination (R^2) of 0.88 and mean squared error (MSE) of 1.39‰ (Figure S11 in Supporting Information S1). This model-data agreement of ECHAM5-wiso has also been demonstrated in previous studies (Hagemann et al., 2006; Werner et al., 2011), highlighting that the model adequately represents the global hydrological cycle and stable isotopic composition. We further compare the model's present-day simulations with observed and reanalysis precipitation and near-surface temperature data sets across West Africa to assess its capability in representing WAM patterns and their seasonality.

3.2. Model Experiments and Boundary Conditions

Previous simulations of Late Cenozoic climate were conducted with different models and model setups. Varied parameterization schemes, spatial resolution, and prescribed boundary conditions complicate the comparison of the regional climates across the considered time periods. We therefore conducted (paleo)climate simulations for PD, PI, MH, LGM, and MP boundary conditions using only ECHAM5-wiso, while maintaining the same spatial resolution. All climate simulation experiments were performed using a high T159 spectral resolution (~80 × 80 km around the equator) and 31 vertical levels up to 10 hPa. The model uses prescribed sea surface temperature (SST) as the interface between the ocean and atmosphere and, therefore, requires less time to reach dynamic equilibrium than fully coupled atmosphere-ocean models. However, the prescribed SSTs disregard oceanic decadal variability, making the simulated response inevitably biased by the specific SST reconstructions used. The paleoclimate experiments were run for 18 years with a 6-hr model output and only considered the last 15 years for the analysis. The first 3 years of the model serve as the spin-up period, which is the time required for the model to reach dynamic equilibrium. Given the study's aim to understand the WAM response to the diverse paleoenvironmental conditions, the different experimental set-ups accounting for variations in orbital parameters, greenhouse gases concentration, SSTs, sea ice concentrations (SICs), and land surface cover (e.g., ice sheet and vegetation) were devised for the different climates. The prescribed boundary conditions for the experiments are similar to the Late Cenozoic simulations presented by Mutz et al. (2018) and Botsyun et al. (2022). We build on those by simulating and analyzing the isotopic compositions for all paleoclimates.

To validate the model's ability to represent WAM dynamics, we compared the present-day (PD) simulation conducted by Boateng et al. (2023) with observed and reanalysis precipitation and near-surface temperature data sets. The PD simulation setup follows the Atmospheric Model Intercomparison Project (AMIP) protocol, using prescribed annual means of SST and SIC from 1979 to 2014. The pre-industrial simulation (the reference year 1850) was also obtained from Boateng et al. (2023). The model was simulated with prescribed SST and SIC from a transient coupled ocean-atmosphere model (Lorenz & Lohmann, 2004). It used an atmospheric CO_2 concentration of 280 ppm in accordance with Dietrich et al. (2013), which was derived from the ice-core record (Etheridge et al., 1996, 1998). Land surface parameters were taken from Hagemann (2002). The initial isotopic composition of the atmosphere was adopted from global gridded data of ^{18}O composition of seawater provided by LeGrande and Schmidt (2006). In this study, the climate change signals are defined as deviations from the PI estimates. Therefore, all reported anomalies (e.g., MH-PI) throughout the paper, described as either "increases" or "decreases," use the simulated PI values as a reference. We also represent the $H_2{}^{18}O$ composition using the δ-notation and calculate it as precipitation-weighted means using the Vienna Standard Mean Ocean Water (V-SNOW).

The SST and SIC boundary conditions prescribed for the MH experiments were derived from transient MH simulation of a low-resolution ocean-atmosphere coupled model (Etheridge et al., 1996, 1998; Lohmann et al., 2013; Wei & Lohmann, 2012). The GHG concentrations (e.g., CO_2 of 280 ppm) are based on ice-core reconstructions (Etheridge et al., 1996, 1998), and the orbital forcing parameters are taken from Dietrich et al. (2013). On the other hand, the LGM simulation was forced with sea surface variables from reconstructions for the Atlantic, Pacific, and Indian oceans based on the GLAMAP (Sarnthein et al., 2003) and CLIMAP (1981) projects. Moreover, the GHG concentrations (CO_2 of 185 ppm) and orbital parameters follow Otto-Bliesner et al. (2006). The paleogeography and ice sheet extent and thickness are based on the PMIP3 experimental protocol (Abe-Ouchi et al., 2015). The vegetation distribution maps for both the LGM and MH are based on the reconstruction of plant functional types from BIOME 6000 of the paleovegetation mapping project (Bigelow et al., 2003; Harrison et al., 2001; Pickett et al., 2004; Prentice et al., 2000). The MP paleoenvironment conditions prescribed in the ECHAM5 model were based on the Pliocene Research, Interpretation, and Synoptic Mapping (PRISM) project (Dowsett et al., 2010; Haywood et al., 2016). More specifically, GHG concentration (e.g., CO_2 of 405 ppm), orbital parameters, land surface variables (e.g., topography, ice cover, and land-sea mask), and sea surface variables (SST, and SIC) were derived from PRISM3D. The vegetation distribution map was regenerated with JSBACH plant functional types using the PRISM reconstruction (Stepanek & Lohmann, 2012). A summary of the major boundary conditions used in this study is presented in Table 1.

Due to the sparse availability of isotopic composition records for the past climates, all the initial conditions of the ocean and the atmosphere were kept the same. The $H_2{}^{18}O$ and HDO starting conditions for the ocean were taken from the equilibrium 3000-year run with MPI-OM-wiso (Xu et al., 2012), and the atmosphere was initialized with $\delta^{18}O$ and δD of −10 and −80‰, respectively, similar to previous studies (e.g., Cauquoin et al., 2019; Werner et al., 2011).

3.3. Observed and Simulated Data Comparison

Reanalysis products are used as validation data sets to assess how ECHAM5-wiso simulates the climatologies and seasonality of precipitation and near-surface temperature across the WAM region. More specifically, the ERA5 climate reanalysis, produced and maintained by ECMWF, is compared to the simulated long-term seasonal means of the PD climate. ERA5 consists of globally interpolated observations (e.g., ocean buoys, satellites, aircraft, weather stations, and other platforms) and numerical simulations using a four-dimensional variational (4D-var) data assimilation scheme (Hersbach et al., 2020). It has hourly output, an approximately 31 km spatial resolution, and extends back to 1959 (Bell et al., 2021). We only extract the monthly long-term mean for the period 1979–2014 due to the simulated time range of the PD experiment. Moreover, the CRU (Climate Research Unit gridded Time series) high-resolution data set (i.e., $0.5° \times 0.5°$ over land regions except for Antarctica), maintained at the University of East Anglia, UK, was used to compare the PD precipitation simulation. CRU relies on the extensive network of global weather stations, which are interpolated using angular-distance weighting (ADW). This data set extends back to 1901 (more details in Harris et al., 2014, 2020).

Table 1
Summary of Boundary Conditions for the ECHAM5-Wiso Experiments (This Study) and the List of PMIP4 Models That Simulated the Coeval Climates

Experiment name	Greenhouse gas concentrations	Orbital forcing parameters	Surface conditions	PMIP4 models considered
Pre-industrial (PI): year 1850	CO_2: 280 ppm, CH_4: 760 ppb, N_2O: 270 ppb.	e: 0.016804, o: 23.4725, lop: 278.734	The SST and SIC data are taken from a low-resolution coupled ocean-atmosphere simulation by Dietrich et al. (2013) and Lorenz and Lohmann (2004). Vegetation distribution data was adopted from Hagemann (2002).	All models
Mid-Holocene (MH): ~6 ka	CO_2: 280 ppm, CH_4: 650 ppb, N_2O: 270 ppb.	e: 0.018682, o: 24.1048, lop: 180.918	SSTs and SICs are obtained from a transient, low-resolution coupled ocean-atmosphere simulation of the Mid-Holocene (Lohmann et al., 2013; Wei & Lohmann, 2012). Vegetation reconstructions from the BIOME 6000 data set (Bigelow et al., 2003; Harrison et al., 2001; Pickett et al., 2004; Prentice et al., 2000) converted into plant functional types.	AWI-ESM-1-1-LR, CESM2, EC-Earth3-LR, GISS-E2-1-G, HadGEM3-GC31-LL, IPSL-CM6A-LR, MIROC-ES2L, NorESM1-F
Last Glacial Maximum (LGM): ~21 ka	CO_2: 185 ppm, CH_4: 350 ppb, N_2O: 200 ppb.	e: 0.018994, o: 22.949, lop: 294.42	SSTs and SICs were derived from GLAMAP reconstructions for the Atlantic Ocean (Sarnthein et al., 2003) and CLIMAP reconstructions for the Pacific and Indian Oceans (CLIMAP, 1981). Land-sea distribution, ice sheet extent, and thickness were based on PMIP3 data (Abe-Ouchi et al., 2015). Vegetation patterns were reconstructed using maps of plant functional types from the BIOME 6000 Paleovegetation Mapping Project (Bigelow et al., 2003; Harrison et al., 2001; Pickett et al., 2004; Prentice et al., 2000) and model predictions provided by Arnold et al. (2009).	AWI-ESM-1-1-LR, CESM2-WACCM-FV2, MIROC-ES2L, MPI-ESM1-2-LR, INM-CM4-8
Mid-Pliocene (MP): ~3 Ma	CO_2: 405 ppm, CH_4: 760 ppb, N_2O: 270 ppb.	e: 0.016804, o: 23.4725, lop: 278.734	SSTs, SICs, land-sea mask, topography, and ice cover data were sourced from PRISM3D (Dowsett et al., 2010; Haywood et al., 2010; Sohl et al., 2009). The vegetation boundary condition was established by converting the PRISM vegetation reconstruction into JSBACH plant functional types, following the method outlined by Stepanek and Lohmann (2012).	CESM2, EC-Earth3-LR, GISS-E2-1-G, HadGEM3-GC31-LL, IPSL-CM6A-LR, NorESM1-F

Note. e stands for eccentricity, o for obliquity, and lop for longitude of perihelion.

3.4. Comparison to PMIP4 Simulations

Simulated model outputs from various climate models that participated in the fourth phase of the Paleoclimate Model Intercomparison Project (PMIP4), which is a component of the current Coupled Model Intercomparison Project (CMIP6) (Eyring et al., 2016), were analyzed to further compare our simulated responses to paleo-environmental conditions with the current state-of-the-art models. However, we emphasize that our analysis does not constitute a formal inter-model comparison since different experimental protocols were used for the simulations in this study. For instance, we rely on a high-resolution atmosphere-only model with prescribed forcings, in contrast to the fully coupled atmosphere-ocean GCMs used in the PMIP4 experiments. Furthermore, the ECHAM5-wiso simulation time is shorter than that of the PMIP4 models (>100 years) due to the longer period required for fully coupled ocean-atmosphere models to reach quasi-equilibrium and avoid drifts in climate variables. The boundary conditions and experimental setup protocols for the PMIP4 models simulating the MH, LGM, and MP are described in Kageyama et al. (2018) and Otto-Bliesner et al. (2017). We analyzed the last 100 years of monthly precipitation amounts for each model, with climate anomalies estimated using their respective PI control simulations. Moreover, we highlight that the individual PMIP4 models' spatial resolutions were kept for our analysis to disentangle the impact of the model resolution in representing the WAM dynamics.

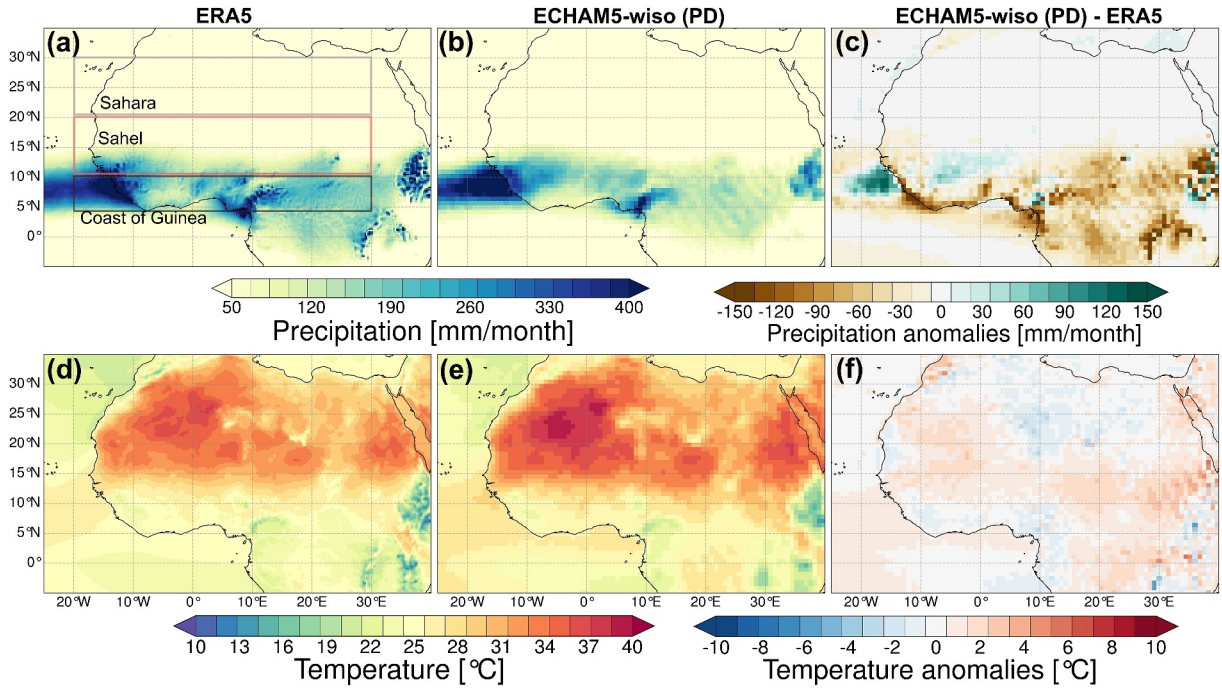

Figure 1. Long-term annual means (1979–2014) of ERA5 and ECHAM5-wiso precipitation (a and b) and near-surface temperature (d and e) during the monsoon season (JJAS), and the differences in precipitation and near-surface temperature between the data sets (c and f). The green color range in the precipitation difference indicates a wet bias, while the brown colors indicate a dry bias in the model. The red color range also represents a warm bias, and the blue colors indicate a cold bias in the model. Overall, the simulated patterns of the rain belt and meridional temperature gradient during the monsoon season demonstrate a reasonable model performance. The demarcated regions in (a) are used for estimating the regional means.

3.5. West African Monsoon Anomalies and Statistical Test

Long-term seasonal means of the WAM months (JJAS) were estimated using the 6-hr model output from the ECHAM5-wiso experiments and the monthly means from the PMIP4 models. The statistical significance of the long-term anomalies is evaluated using a student *t*-test with a confidence interval threshold of 95%. It is important to note that the analysis is based on uncorrected time, even though orbits were modified in the time slice experiments. However, this does not influence the analysis since climatological means are considered. As the WAM seasonality is zonally distributed (Janicot et al., 2011; S. E. Nicholson & Palao, 1993), three different latitudinal transects were delineated for further analysis. Specifically, zonal averages over the Sahara (30–20°N, 20°W–30°E), Sahel (20–10°N, 20°W–30°E), and Guinea coast (10–5°N, 20°W–30°E) were used to understand the meridional variations of the simulated rain belt across the WAM region.

4. Results

4.1. Present-Day Simulation and Comparison to Observations

Comparisons of the simulated and the observed spatial patterns and seasonality of precipitation and near-surface temperature revealed that ECHAM5-wiso represents the climate across the WAM region well. More specifically, the simulated and observed precipitation in the monsoon season shows a similar rain belt, that is, a latitudinal band of maximum precipitation of approximately 400 mm/month across Africa. There are only slight deviations in magnitude between ECHAM5-wiso and ERA5 (Figures 1a–1c): ERA5 shows a higher magnitude of precipitation, with ∼40 mm/month more than predicted by the simulation. However, comparing the simulated patterns to the CRU data sets reduces these slight differences in precipitation patterns and magnitudes (Figure S1 in Supporting Information S1). Moreover, the simulated near-surface temperature indicates similar spatial patterns with a pronounced meridional gradient, indicating high temperatures of up to 40°C across the Sahara region (Figures 1d–1f).

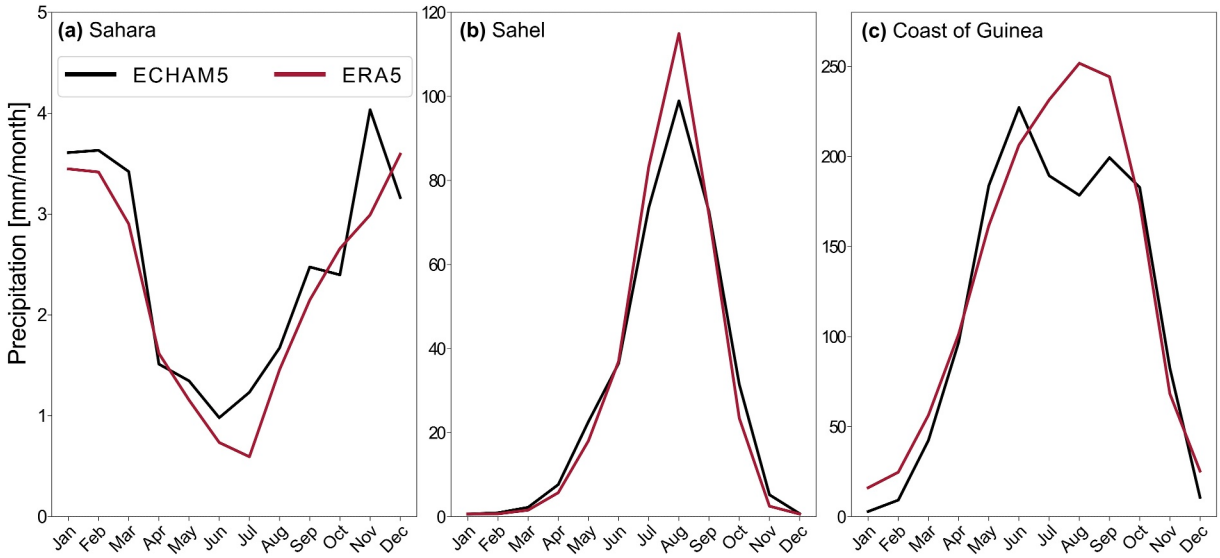

Figure 2. Comparison of ERA5 (red) and ECHAM5-wiso (black) monthly precipitation changes across the (a) Sahara (30–20ºN, 20ºW–30ºE), (b) Sahel (20–10ºN, 20ºW–30ºE), and (c) Coast of Guinea (10–5ºN, 20ºW–30ºE) (see Figure 1a). For the Sahara and the Sahel, the modeled evolution of the WAM is consistent with ERA5. However, the model produces the expected bimodal precipitation seasonality across the Guinea coast, while ERA5 only shows a unimodal pattern.

The migration of the WAM drives different seasonal precipitation patterns across West Africa. Consequently, we analyze the seasonal trends using regional monthly means across the Sahara, Sahel, and the coast of Guinea. Overall, the model simulates an accurate seasonal distribution and intensity across most of the transects (Figure 2). Specifically, the observed and the modeled seasonal cycle shows a precipitation increase of >3 mm/month during the winter in the Sahara region (Figure 2a). Moreover, the model also simulates a realistic unimodal monthly distribution across the Sahel, with maximum precipitation of ∼100 mm/month in August (Figure 2b). However, ECHAM5-wiso predicts the expected bimodal precipitation seasonality across the Guinea coast, with peak months in June (∼225 mm/month) and September (∼200 mm/month), while ERA5 indicates wider unimodal patterns of maximum precipitation of ∼250 mm/month in June (Figure 2c). Despite the adequate precipitation representation of ERA5 over West Africa, previous studies have indicated their underestimation over the coast of Guinea (e.g., Quagraine et al., 2020). Overall, the present-day simulation results confirm ECHAM5-wiso's ability to represent the hydroclimate of the WAM and its associated teleconnections, validating its use for paleoclimate simulations.

4.2. Simulated Changes of the WAM in the Late Cenozoic

The simulated regional patterns of the WAM in the MH, LGM, and MP deviate significantly from PI conditions. Overall, the model estimates an intensification of the WAM in the MH and MP, with the MH showing a more significant intensification than the MP. On the other hand, the model estimates a pattern of extensive dryness during the WAM season in the LGM (Figure 3). The estimated precipitation anomalies during the WAM season in the MH indicate bidirectional latitudinal patterns. The MH experiment estimates an increase of ∼150 mm/month from 7° to 30°N, with statistical significance below 27°N. Conversely, the model indicates a decrease of ∼30 mm/month toward the coastal regions (2–6°N) (Figure 3a). Overall, the LGM simulation indicates a precipitation decrease of up to 150 mm/month across the WAM region, with significant anomalies along the coastal regions (Figure 3b). Lastly, MP estimates an increase of ∼100 mm/month in precipitation anomalies during the WAM season, with patches of a slight decrease in precipitation along the coast of Guinea, Nigeria, and Cameroon (Figure 3c). The simulated patterns of precipitation anomalies indicate a higher magnitude of the latitudinal extent of the WAM toward the Sahara region in the MH compared to the MP. To assess the relative importance and added value of using ECHAM5-wiso to simulate all the studied periods, we compare our model estimates to those of other models from the CMIP6-PMIP4 experiments (Table 1) that simulate the same periods. We focus our analysis on regional means of precipitation anomalies across the Sahel and also evaluate the latitudinal distribution of the WAM. The simulated WAM seasonal climatologies of the different climates (i.e., MH, LGM, and

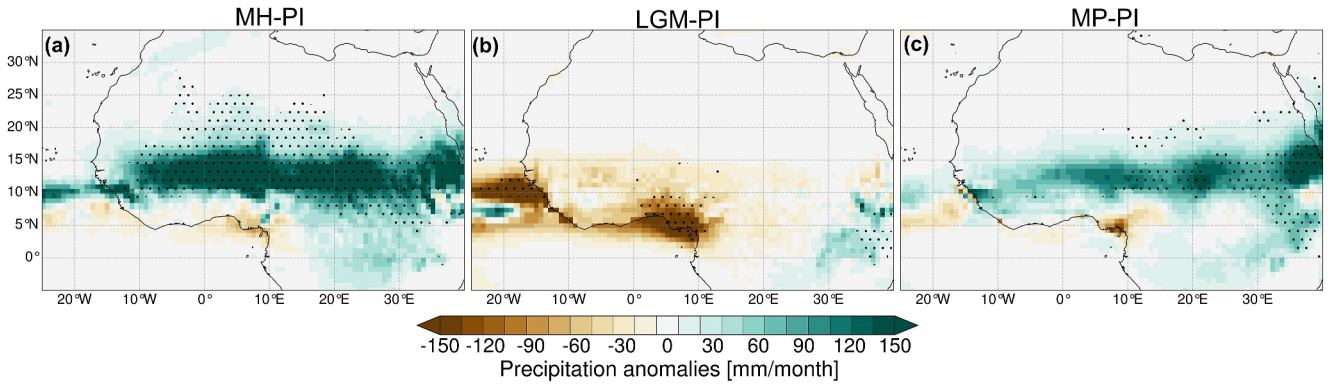

Figure 3. Precipitation anomalies during the WAM season (JJAS) for the (a) Mid-Holocene (MH), (b) Last Glacial Maximum (LGM), and (c) Mid-Pliocene (MP), as simulated by ECHAM5-wiso. The green color range represents wetter conditions, while the brown color range represents drier conditions compared to the Pre-Industrial (PI) estimates. The black dot stippling indicates regions with statistically significant differences, assuming a confidence interval of 95% based on a student *t*-test analysis. The precipitation anomalies patterns indicate the highest intensification of the WAM and its northward reach in the MH despite the enhanced hydrological cycle in the MP.

MP) and their respective control means (PI) are presented in the supplementary material (Figures S2, S3, S4, and S5 in Supporting Information S1).

Overall, the inter-model comparison reveals consistent estimates in the direction and magnitude of change in response to different paleoenvironmental conditions, with the exception of CESM2-WCCM-FV2. Surprisingly, this model estimates an increase in precipitation anomalies across the Sahel in the LGM (Figure 4b). However, Zhu et al. (2021) have indicated that this unrealistic sensitivity to colder climates may be attributed to exaggerated shortwave cloud feedback or an unrepresented physical mechanism countering such cloud feedback. Specifically, ECHAM5-wiso estimates the maximum increase in precipitation anomalies of ∼90 mm/month across the Sahel in the MH for the WAM season, followed by MPI-ESM1-2-LR (with ∼80 mm/month), while GISS-E2-1-G shows the lowest precipitation anomalies of ∼35 mm/month (Figure 4a). Alternatively, AWI-ESM-1-1-LR estimates a maximum precipitation decrease of 55 mm/month across the Sahel in the LGM (Figure 4b). The precipitation decreases (∼20 mm/month) estimated by ECHAM5-wiso is similar to the estimates by the INN-CM4-8 and MIROC-ES2L models. In the MP, the WAM response across the Sahel exhibits a wider range of precipitation anomalies, with EC-Earth3-LR, indicating the maximum increase of ∼160 mm/month and GISS-E2-1-G showing the lowest increase of ∼10 mm/month (Figure 4c). However, ECHAM5-wiso estimates fall within a mid-range of ∼50 mm/month, which is closer to the estimates by HadGEM3-GC31-LL, IPSL-CM6A-LR, and NorESM1-F models. Even though ECHAM5-wiso indicates a maximum intensification of the WAM across the Sahel in the MH rather than in the MP, other models (e.g., EC-Earth3-LR) suggest the reverse trend. Consequently, the longitudinal regional means of the latitudinal distribution of precipitation anomalies during the WAM season are evaluated to compare the northward migration of the WAM in response to the different paleoenvironments (Figure 4).

In total, most of the PMIP4 models suggest a higher meridional migration of the WAM in the MP than in the MH, while the magnitude of changes in the latitudinal band of maximum precipitation varies among the individual models (Figure 5). Specifically, EC-Earth3-LR estimates maximum latitudinal precipitation of 200 mm/month with a greater northward extent in MP than the ∼100 mm/month rain belt in the MH (Figures 5a and 5c). However, GISS-E2-1-G suggests a higher intensification of the WAM with an increase in precipitation by 50 mm/month in the MH, and a relatively modest increase of ∼10 mm/month in the MP (Figures 5a and 5c). The ECHAM5-wiso experiments suggest a slight northward extent of the WAM in the MH and a higher intensification (∼80 mm/month more) than in the MP (Figures 5a and 5c). Despite the estimated differences, all the models, including ECHAM5-wiso, indicate a similar meridional distribution in the MH and MP. However, CESM2-WCCM-FV2 and INM-CM4-8 distinctively suggest an increased distribution of meridional precipitation anomalies across the WAM areas and toward the equatorial Atlantic in the LGM (Figure 5b), respectively, despite the general decreasing trend estimated by the other models.

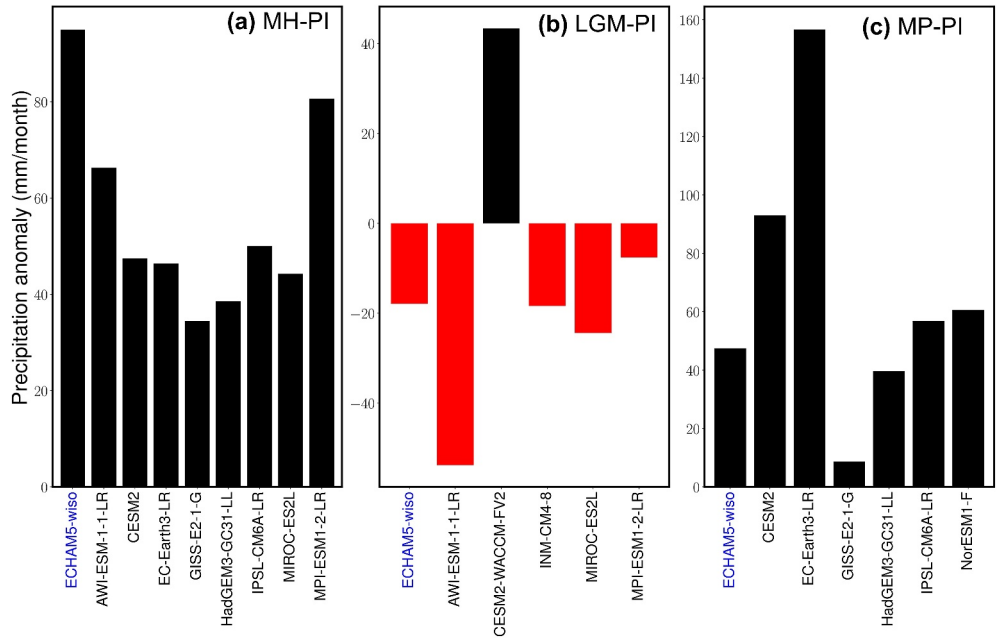

Figure 4. Regional means of precipitation anomalies during the WAM season estimated for the Sahel region (see Figure 1a) using ECHAM5-wiso (labeled in blue) and the PMIP4 models considered (Table 1) for the (a) Mid-Holocene (MH), (b) Last Glacial Maximum (LGM), and (c) Mid-Pliocene (MP) paleoenvironmental conditions. The individual precipitation anomalies are estimated based on their respective pre-industrial (PI) runs.

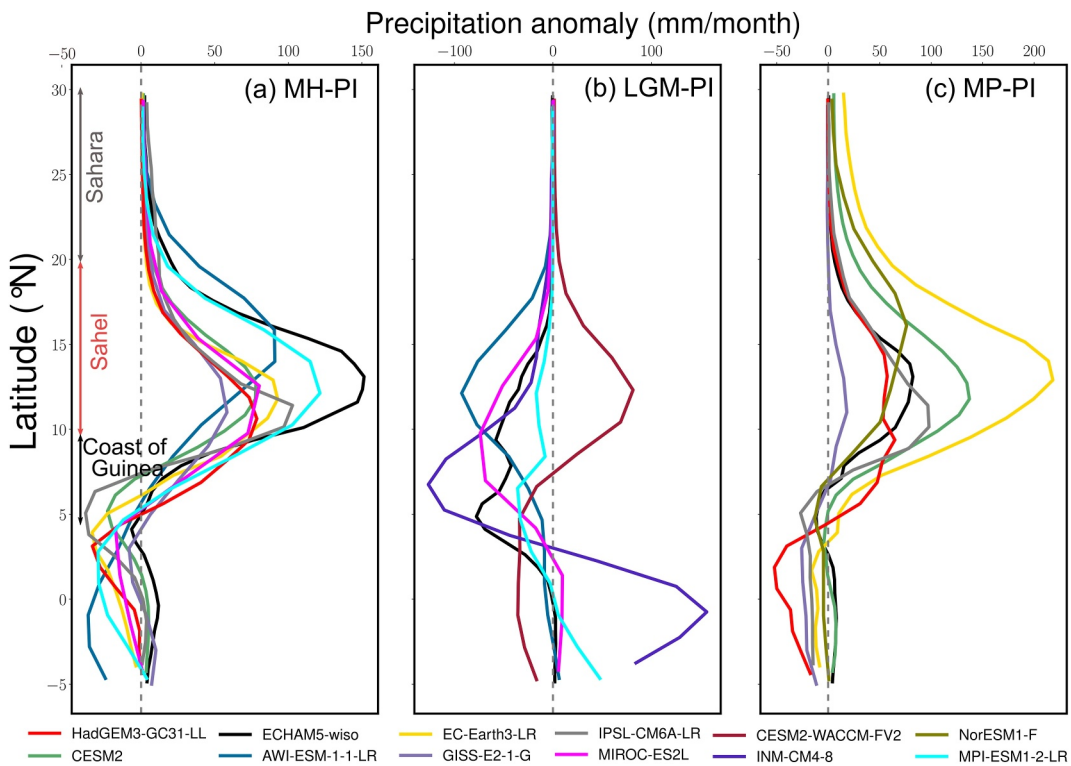

Figure 5. Latitudinal regional, seasonal means (JJAS) of precipitation anomalies across the WAM region (averaged between 20°W and 30°E) estimated for the ECHAM5-wiso and PMIP4 models for (a) Mid-Holocene (MH), (b) Last Glacial Maximum (LGM), and (c) Mid-Pliocene (MP) simulations. ECHAM5-wiso estimates show a latitudinal distribution that is consistent with most of the PMIP4 models. ECHAM5-wiso estimates for LGM and MP fall into the PMIP4 model range, while ECHAM5-wiso estimates for the intensification of the WAM in the MH exceed the PMIP4 model range.

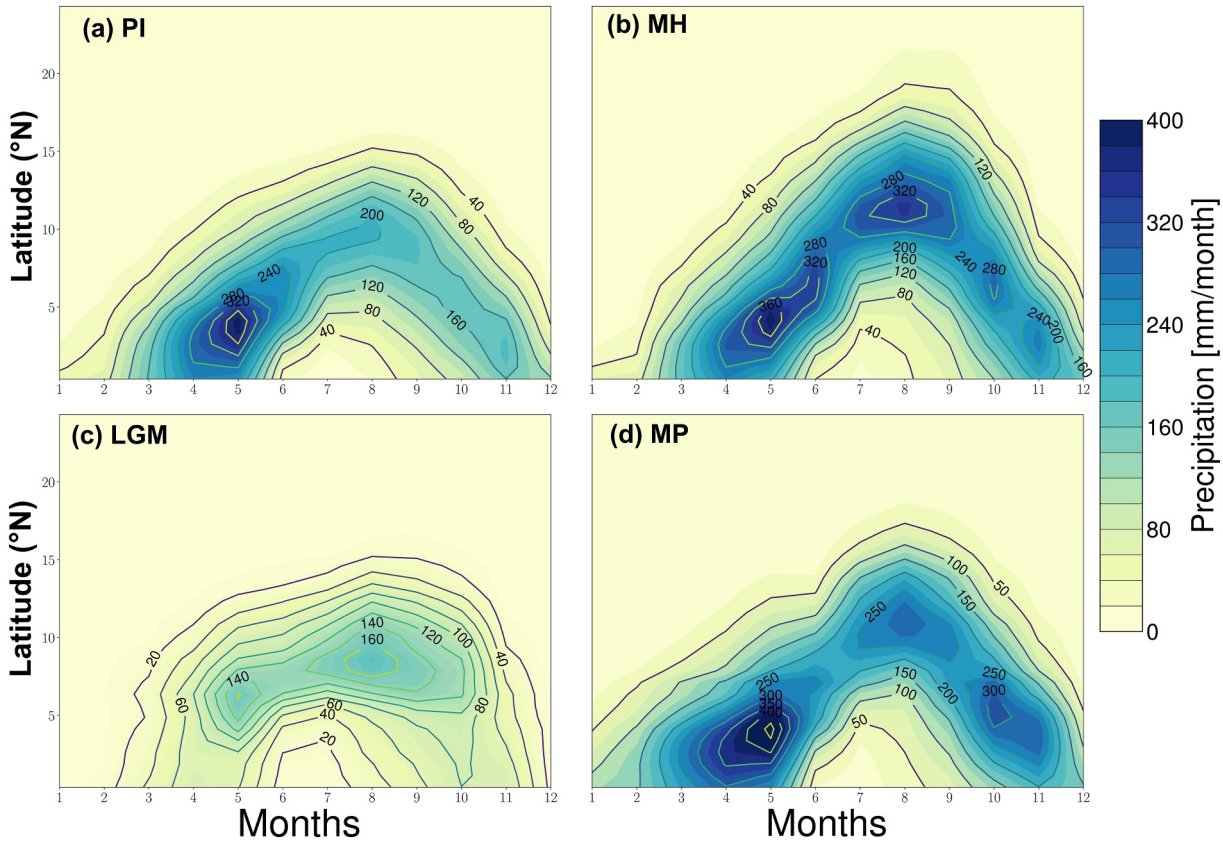

Figure 6. Hovmöller diagram (space-time) showing the latitudinal seasonal migration of precipitation across the WAM region (averaged between 20°W and 30°E) for the (a) Pre-industrial (PI), (b) Mid-Holocene (MH), (c) Last Glacial Maximum (LGM), and (d) Mid-Pliocene (MP) experiments using ECHAM5-wiso. The MH seasonal distribution indicates the highest precipitation rate during the high-rainfall period (June-August), while the MP indicates more precipitation in the onset (March-May) and southward retreat (September-October) periods.

4.3. Seasonality of the Simulated WAM in the Late Cenozoic

The meridional migration of the WAM is investigated by analyzing the evolution of latitudinal regional means (Hovmöller diagram) (Figure 6) and regional means over the coast of Guinea, Sahel, and Sahara (Figure 7). Generally, the seasonal cycle of the WAM progresses from two rainy season regimes across the coastal areas to a single rainy event across higher latitudes (Figure 2). The progression of the WAM is classically defined in three phases: (a) the onset period (March-May), driven by the low-level south-westerlies moist transport from the South Atlantic toward the coastal regions up to 4°N and the abrupt shift of the ITCZ from the quasi-stationary zone between 5 and 8°N to 8–10°N, (b) the high rain period (June–August), which abruptly shifts the rain belt up to 10°N (also known as monsoon jump), marking the start of the high rainfall events in the Sahel and the end of the first rainy regime across the coast, and (c) the southward retreat (September-October), reflecting the last phase of the WAM annual cycle and the second rainfall region across the coast (Barbé et al., 2002; Sultan et al., 2003; Sultan & Janicot, 2003).

The latitudinal evolution of the WAM in the PI indicates maximum precipitation of up to 320 mm/month during the onset period (from March to May) along the coast, followed by a monsoonal jump up to 15°N in the Sahel with ≤40 mm/month of precipitation (Figure 6a). Moreover, the southward retreat toward the coast at the end of the annual cycle records half of the precipitation (i.e., ∼160 mm/month) during the onset period. The MH evolution exhibits similar phases, but with higher precipitation and a greater northward extent. Specifically, the onset period records precipitation of ∼360 mm/month and a higher northward shift up to ∼25°N with higher precipitation rates of up to 320 mm/month across the Sahel (Figure 6b). The southward retreat phase in the MH is also characterized by higher precipitation rates of up to 240 mm/month. Overall, the MP seasonal trend shows an inverted V-shape distribution that is similar to the MH pattern, but flatter and with a higher rainfall in the onset and southward

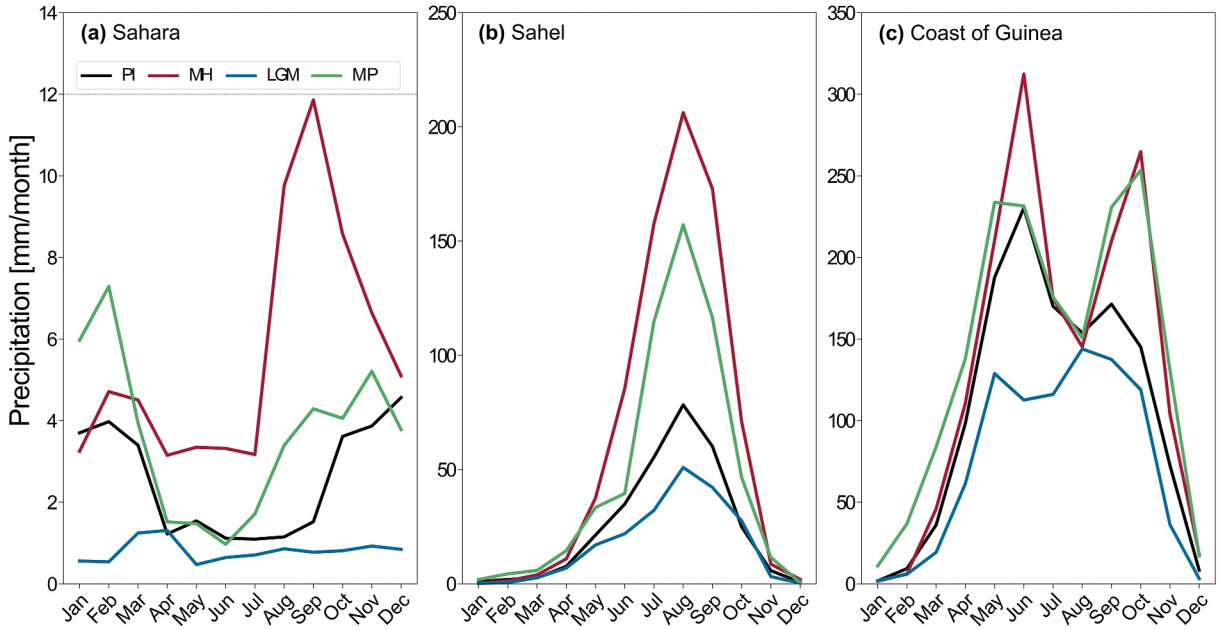

Figure 7. Seasonal cycle of precipitation across the (a) Sahara (30–20°N, 20°W–30°E), (b) Sahel (20–10°N, 20°W–30°E), and (c) Guinea coast (10–5°N, 20°W–30°E) (See Figure 1a) estimated for the Pre-industrial (PI; black), Mid-Holocene (MH; red), (c) Last Glacial Maximum (LGM; blue), and (d) Mid-Pliocene (MP; green) simulation using ECHAM5-wiso. The seasonal distribution of precipitation across the Sahara shows different peak months for the different past climates, while the Sahel and Coast of Guinea show a more consistent seasonality.

retreat phases along the coast. The onset and southward retreat phases are characterized by precipitation rates of ∼400 mm/month and 300 mm/month across the coast of Guinea and the equatorial Atlantic, respectively (Figure 6d). However, the high-rainfall period is characterized by less rainfall (∼250 mm/month) across the Sahel and a lower latitudinal extent (≤18°N) when compared to MH. On the other hand, the LGM simulations predict drier conditions in all seasons, with a rainfall increase of only up to 160 mm/month in the Sahel during the high-rain period (Figure 6c).

The seasonal cycle across the different climate zones is assessed through their regional means. The seasonal precipitation cycle exhibits pronounced variations in magnitude, but few changes in precipitation distribution (Figure 7). Among those few changes are variations in peak precipitation months estimated for the Sahara. While the PI estimates indicate higher precipitation (∼4 mm/month) in November-February, the MH estimates suggest more precipitation from July to October, with peak precipitation rates of 12 mm/month in September. Overall, the LGM estimates indicate persistently drier conditions across all seasons in the Sahara. The MP also indicates a higher precipitation record in the pre-onset period across the Sahara, with a peak month in February (∼7 mm/month). Regarding the bimodal monthly distribution along the coastal regions, all climates show similar patterns. For the MH, the precipitation peaks are highest, that is, a ∼300 mm/month peak in June and a ∼260 mm/month peak in October. The estimates across the Sahel also exhibit a unimodal distribution and precipitation peak in August. The MH simulation produces the highest peak, with an increase of more than 100% relative to the PI.

4.4. Changes of Stable Oxygen Isotopic Composition in Precipitation Associated With Late Cenozoic Changes in the West African Monsoon

In this section, we explore the simulated seasonal climatological anomalies of the precipitation-weighted stable oxygen isotopic composition of precipitation ($\delta^{18}O_p$) during the WAM season (Figure 8). Even though $\delta^{18}O_p$ values are closely linked to precipitation due to the "amount effect", the simulated spatial patterns of precipitation and $\delta^{18}O_p$ values are different. Overall, the warmer climates (i.e., MH and MP) estimate a decrease in $\delta^{18}O_p$ values across the WAM region when compared to the PI patterns during the monsoon season (Figures 8a and 8c). In contrast, the $\delta^{18}O_p$ anomalies increase across many parts of the WAM region in response to the colder conditions in the LGM (Figure 8b). The MH is characterized by a significant decrease of $\delta^{18}O_p$ values by $\sim -5‰$ between 10 and 20°N, which spatially coincides with the region of the rain belt (Figure 8a). The decrease becomes

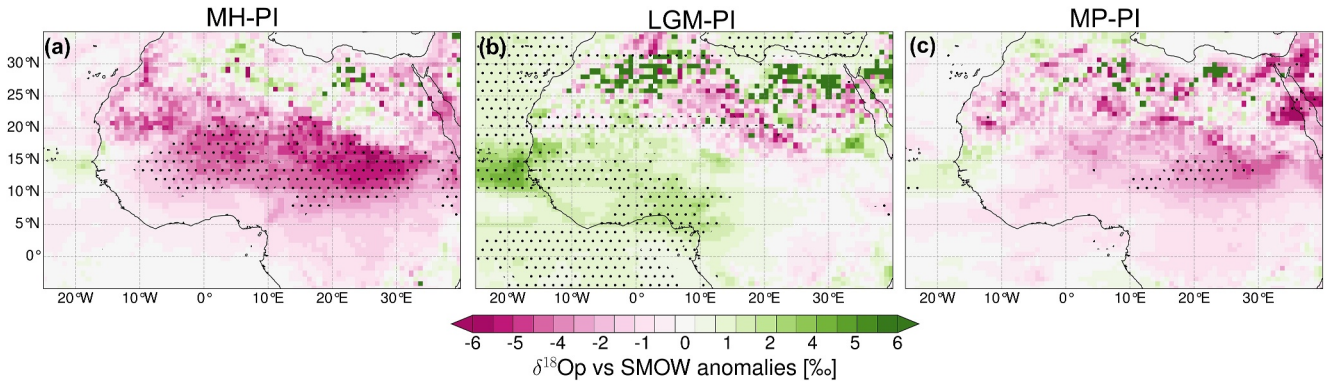

Figure 8. Simulated changes in $\delta^{18}O_p$ in the WAM season (JJAS) for the (a) Mid-Holocene (MH), (b) Last Glacial Maximum (LGM), and (c) Mid-Pliocene (MP). The pink color range represents heavy isotope depletion, and the green color range represents an enrichment in the heavy isotopes in relation to Pre-industrial (PI) values. The black dot stippling indicates regions with a statistically significant difference, assuming a confidence interval of 95%, using a student *t*-test analysis.

less pronounced (∼−1‰) toward the Sahara region, and shows small areas that experience a slight increase (∼1‰) toward the east. Moreover, the equatorial Atlantic region also experiences a slight $\delta^{18}O_p$ decrease of about 1‰. The $\delta^{18}O_p$ anomalies during the MP also decrease across the continent, but show an increase of up to −6‰ across the Sahara (Figure 8c). Furthermore, the decrease of $\delta^{18}O_p$ values across the Sahel is less significant than the increase in precipitation anomalies in the MP. On the other hand, the LGM simulation indicates a significant increase in $\delta^{18}O_p$ values of ∼3‰ across the Atlantic Ocean and the adjacent coastal regions (Figure 8b).

4.5. Changes in the Atmospheric Dynamics Behind the Simulated WAM Changes

Here, we analyze the atmospheric dynamics behind the simulated changes in the WAM. Specifically, we use near-surface temperature, mean sea level pressure, wind patterns at different atmospheric levels, and surface heat fluxes to investigate how these dynamics change in response to different late Cenozoic boundary conditions. Due to our current understanding of WAM dynamics (Section 2.1), we focus on the spatial and intensification changes of the surface temperature and pressure gradients, AEJ, TEJ, and the low-level south-westerly winds as the dynamic feedback contributing to the simulated changes in the WAM. Additionally, we evaluate the changes in the WAM due to land surface conditions (e.g., prescribed vegetation) in the experiments through the responses of surface latent and sensible heat fluxes.

4.5.1. Changes in Near-Surface Temperature

The warmer climate experiments (i.e., MH and MP) produce a north-south near-surface temperature gradient with an increase in the Sahara region, a decrease in the Sahel, and smaller regions of increases (MP) or no (MH) changes at the southern coast (Figure 9). Overall, the MH indicates a pronounced meridional gradient with a significant increase in temperature anomaly of up to 10°C across the Sahara and a significant decrease of down to −8°C toward the Guinea coast (Figure 9a). The MP anomalies indicate similar patterns, but with less pronounced gradients and significant changes only toward Central and East Africa. More specifically, the MP shows an increase of up to 5°C across the Sahara and a decrease of about −3°C across the Sahel, transitioning into a slight increase of up to 2°C in the equatorial Atlantic (Figure 9c). This spatial variability is consistent with the precipitation patterns. Moreover, the mean sea level pressure patterns also indicate the deepening of the low-pressure area across the Sahara in MH compared to the MP (Figure S6 in Supporting Information S1). However, comparing the cyclonic flow across the Sahara and the strengthened south-westerlies moist transport from the equatorial Atlantic at 850 hPa between the MH and MP reveals no noticeable changes (Figure S6 in Supporting Information S1). Contrarily, the temperature anomalies in the LGM indicate overall colder conditions across the continent with a significant decrease of up to −5°C.

4.5.2. Changes in the Vertical Structure of Zonal and Meridional Wind Speeds

We analyzed the latitudinal-altitude cross-sections of zonal and meridional wind speeds across the WAM region to understand the atmospheric circulation associated with the simulated precipitation dynamics. The zonal wind

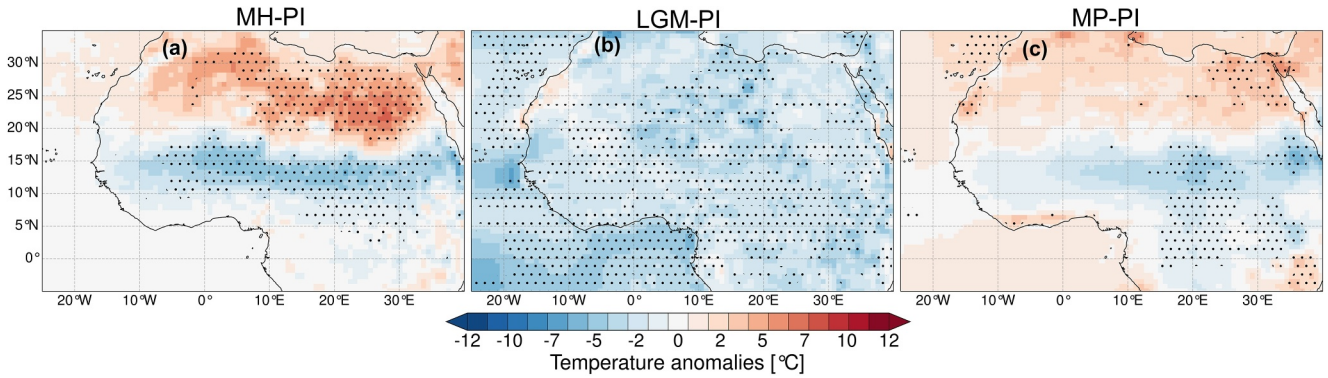

Figure 9. Simulated temperature anomalies of the WAM season (JJAS) estimated in response to the (a) Mid-Holocene (MH), (b) Last Glacial Maximum (LGM), and (c) Mid-Pliocene (MP) paleoenvironmental conditions using ECHAM5-wiso. The blue color ranges represent colder conditions, and the red color ranges represent warmer conditions compared to the pre-industrial estimates. The black dot stippling indicates regions with a statistically significant difference, assuming a confidence interval of 95% using a student *t*-test analysis.

patterns reveal a higher altitudinal reach of the low-level southwesterlies and a greater northward propagation in the MH and MP when compared to the PI and LGM (Figure 10). The westerlies reach a latitudinal extent of 17°N and stay below 800 hPa atmospheric level in the PI and LGM, while in the MH and MP, the flows extend over 20°N and up to the 700 hPa level (Figures 10a–10d). The MH and MP simulations estimate a higher northward reach of the winds, but the latter predicts slightly higher wind shear at the core of the low-level flow. Consistently,

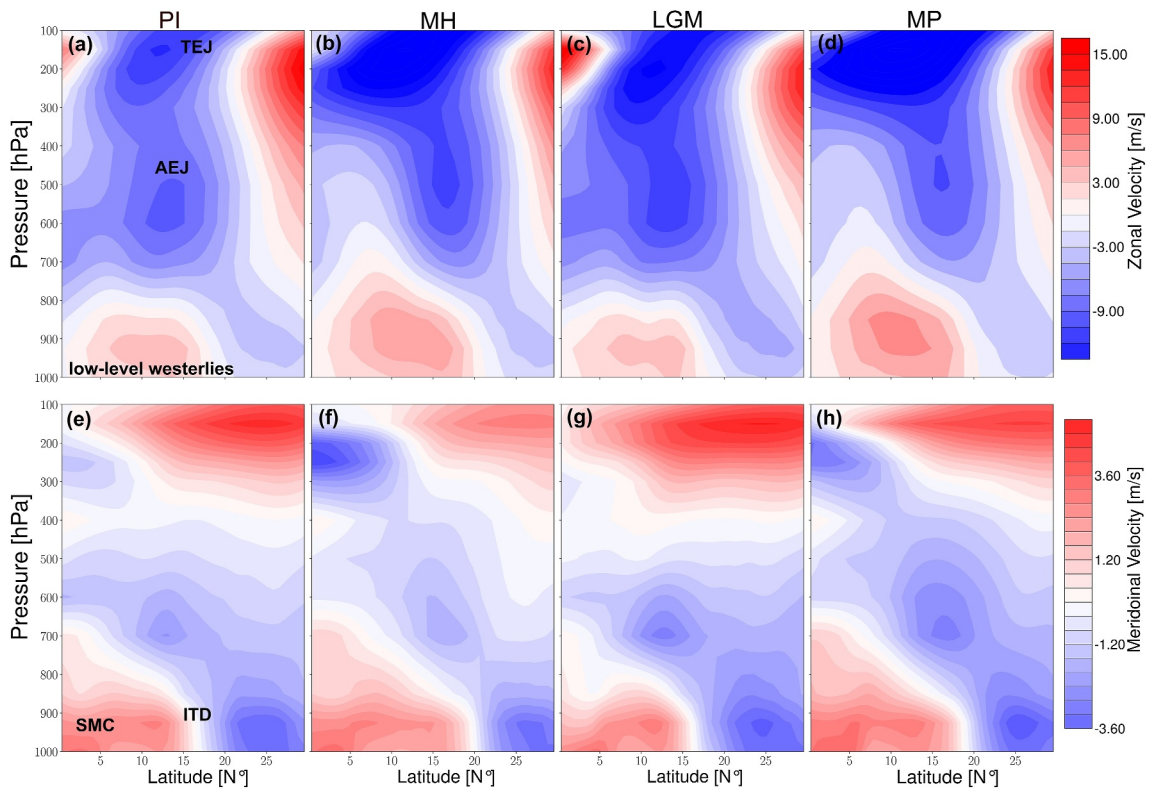

Figure 10. Latitudinal vertical cross-sectional for zonal (top panel) patterns, where positive (negative) values indicate westerly (easterly) winds, and for meridional patterns (bottom panel), where positive (negative) values indicate southerly (northerly) wind speeds estimated for the WAM season (JJAS) in response to (a) Pre-industrial (PI), (b) Mid-Holocene (MH), (c) Last Glacial Maximum (LGM), and (d) Mid-Pliocene (MP) paleoenvironmental conditions. The approximate locations of the African Easterly Jet (AEJ), Tropical Easterly Jet (TEJ), Intertropical Discontinuity (ITD), low-level westerlies and Shallow Meridional Cell (SMC) are shown in a and e. The low-level westerlies reach the highest latitude and altitude in the MH. The strengthened WAM conditions are more associated with the northward position of the Africa Easterly Jet (AEJ) than its intensity.

the AEJ is located between 10 and 15°N at approximately 600 hPa in the PI and LGM. However, the LGM indicates a more intense AEJ than the PI despite overall drier conditions. In the MH and MP, the AEJ experiences a greater northward shift between 15 and 20°N, and its core shifts to a higher altitude than in the PI. In contrast to the LGM and PI, the AEJ in the MH indicates higher intensification than the MP.

The latitudinal-altitude cross-section of winds also indicates higher vertical wind shear (inferred from the transition from the low-level westerlies to the mid-level easterlies) in the MH and MP compared to the PI. Stronger southwesterlies (and, therefore, a deeper monsoon depth) are also identified in the MH and MP. The monsoon depth defines the altitudinal reach of moisture transport from the equatorial Atlantic into the continent. In contrast, the LGM experiment estimates a shallow monsoon depth compared to the PI. More specifically, the monsoon depth reaches an altitude of 600 hPa in the MH and MP, and only up to 700 hPa in the PI and LGM (Figures 10e–10h). Moreover, the patterns in the MH and MP indicate a more northward location of the ITD (i.e., the location where the moist southwesterlies deflect the dry northeasterlies from the Sahara) at approximately 20° and 19°N, respectively. For the PI and LGM, the ITD is located further south (<17°N). The intensity of the low-level moisture transport, TEJ, AEJ, and the location of the ITD coincide with the latitudinal band of negative omega values (wind directions away from the ground; updraft) up to 200 hPa and the associated subsidence (positive omega values) across the Sahara (Figure S7 in Supporting Information S1). Overall, the tropospheric structure of the winds reveals stronger southwesterlies moisture transport from the tropical Atlantic, a higher monsoon depth, the northward position of the AEJ, and the intensification of the TEJ, consistent with the increased intensity of the WAM and its northward migration in the MH and MP.

4.5.3. Changes in Sensible and Latent Heat Fluxes

Generally, high vegetation cover yields more water availability through evapotranspiration, which increases latent heat (LH) flux. Moreover, moisture availability due to the increased LH flux leads to a rainfall-induced cooling effect, reducing sensible heat (SH) flux into the atmosphere. Specifically, for the WAM region, the recycling of water vapor through evaporative fluxes also contributes to the northward extent of precipitation. Therefore, the response of the WAM to different surface conditions is described here through the analysis of SH and LH fluxes. However, we highlight that diagnosing the causes of the changes in terrestrial water balance (i.e., precipitation minus evaporation) through moisture budget analysis (Seager & Henderson, 2013) will help better quantify the contribution of the atmospheric circulation and surface moisture fluxes to the precipitation changes (e.g., Feng et al., 2022) and will be addressed in future study.

The paleoclimate experiments indicate varied responses to the surface heat fluxes (Figure 11). In the MH experiment, the results indicate pronounced negative LH anomalies (i.e., upward flux) of up to -80 Wm^{-2} across the Sahel, gradually reducing in magnitude towards the Sahara (Figure 11a). Regions with more upward LH fluxes coincide with regions of a significant increase in precipitation the MH. The LGM reveals overall positive (downward) LH flux anomalies across the Sahel and coastal regions, with no changes towards the Sahara due to colder and drier conditions (Figure 11b). In the MP, the estimated patterns reveal a slight increase in upward fluxes with negative LH anomalies down to -30 Wm^{-2} across the Sahel, and no changes in the Sahara (Figure 11c). Such simulated patterns of releasing LH are consistent with higher enhanced evaporation over vegetated surfaces through radiative forcing (Figure S8 in Supporting Information S1) in the MH. The SH flux anomalies also show consistent results with more downward fluxes and colder surface conditions associated with increased precipitation. The MH experiment estimates negative SH anomalies down to -60 Wm^{-2} across the Sahara, reaching 15°N and positive SH anomalies across the Sahel towards the coastal regions (Figure 11d). The zonal band of the downward SH anomalies is also consistent with the simulated rain belt in both the MH and MP. The MP experiment estimates a similar, albeit less pronounced, north-south gradient of SH. The LGM experiment estimates negative SH anomalies across most regions on the continent, which is consistent with less availability of water to evaporate. The simulated SH flux patterns are consistent with the near-surface temperature anomalies, with a more pronounced meridional gradient in the MH relative to the MP.

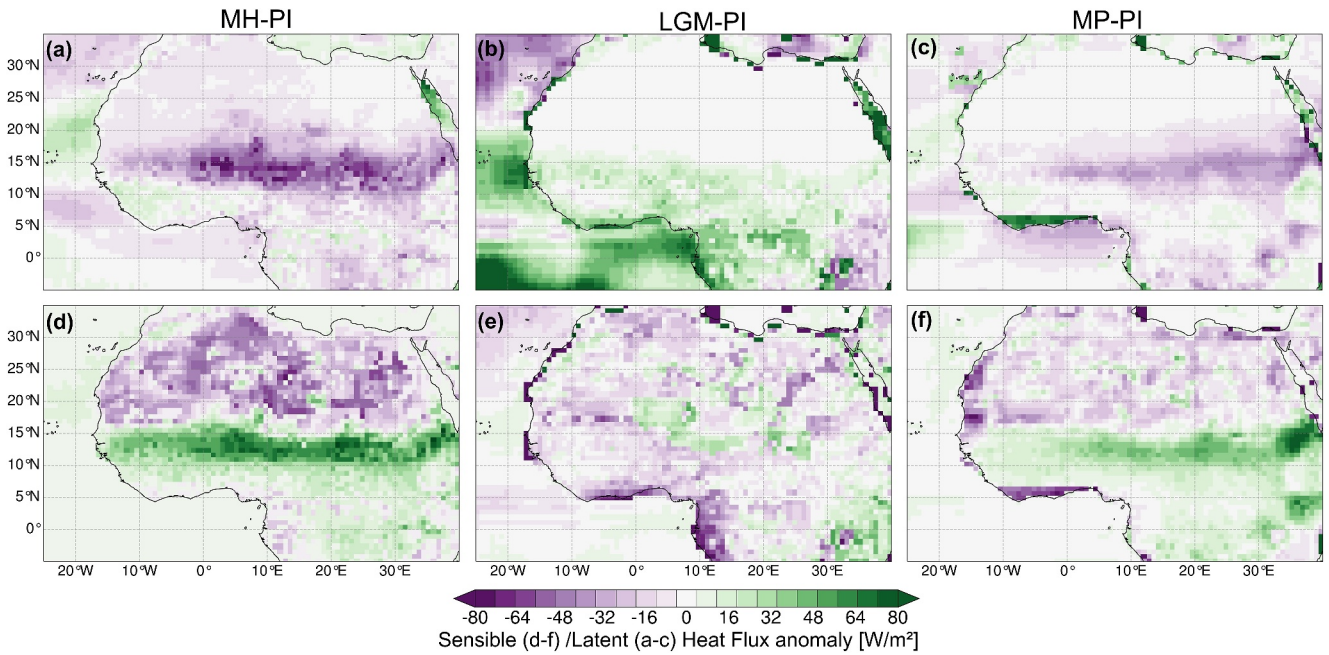

Figure 11. Latent (top panel) and Sensible (bottom panel) heat flux anomalies during the WAM months (JJAS) for the (a) Mid-Holocene (MH), (b) Last Glacial Maximum (LGM), and (c) Mid-Pliocene (MP). The purple ranges represent net upward fluxes, and the green color ranges represent downward fluxes.

5. Discussion

5.1. Simulated Changes of the WAM in Response to the Large-Scale Forcings

5.1.1. Mid-Holocene (~6 ka)

Overall, the analyzed climate model outputs consistently indicate the intensification and expansion of the WAM during the MH, specifically during the boreal summer. These simulated patterns align with findings from previous modeling studies (e.g., Bosmans et al., 2012; Gaetani et al., 2017; Patricola & Cook, 2007; Zhao & Harrison, 2012) and proxy reconstructions (e.g., Bartlein et al., 2011). The increase in precipitation during the WAM season is not surprising, given that the orbital configurations of the MH lead to stronger insolation during the boreal summer and autumn, and to weaker insolation during the winter when compared to PI forcings (Joussaume et al., 1999; Kutzbach & Liu, 1997). These orbital precision variations with stronger seasonal thermal amplitudes also result in more pronounced equator-to-pole and land-sea thermal gradients, contributing to moisture redistribution across the continents (Brierley et al., 2020). Specifically, the stronger thermal gradients and associated continental warming during the WAM season (JJAS) deepen the low-pressure cells over the Sahara. This intensifies the advection of moist air masses from the equatorial Atlantic Ocean, thereby amplifying and expanding the WAM. Moreover, the redistribution of moisture associated with the seasonal insolation distribution can be observed as a weakening of the annual-scale range of precipitation over the ocean and a strengthening over the continent, as suggested in previous studies (e.g., Braconnot et al., 2004). The MH precipitation anomalies in the inter-annual scale are less pronounced than the seasonal changes. These changes reflect that the seasonal variations in insolation primarily drive the MH global climate changes (Kageyama et al., 2013). The ECHAM5-wiso model estimates global warming of approximately ~0.3°C compared to the PI control run (Figure S9 in Supporting Information S1). The bidirectional precipitation anomalies, with drier conditions toward the coastal regions, are also consistent with the rainfall dipole patterns of the African Humid Period (AHP). This phenomenon is explained by the northward shift of the ITCZ during the boreal summer in response to the insolation in the Northern Hemisphere (Braconnot et al., 2007; Coe & Harrison, 2002; deMenocal et al., 2000).

Compared to the model outputs from the PMIP4-CMIP6 experiments, ECHAM5-wiso predicts the highest intensification and greatest northward reach of the WAM. The precipitation anomalies estimated with ECHAM5-wiso indicate a maximum rain belt of approximately 150 mm/month across the Sahel (10–20°N) and less rainfall reaching 30°N. Out of all considered models, ECHAM5-wiso estimates predict the highest regional precipitation

means (~95 mm/month), followed by the MPI-ESM-LR, which has a similar atmospheric model component (i.e., ECHAM6). This also further validates the ability of models in the ECHAM family to reproduce the atmospheric dynamics and hydrological cycle across the African continent. The relatively high precipitation rates predicted by our ECHAM5-wiso simulations might be partly due to the following:

1. The representation of MH vegetation feedbacks. The experimental design for the PMIP4-CMIP6 MH simulation keeps vegetation from the PI, using prescribed surface conditions or dynamic vegetation models. However, previous studies have suggested a "Green Sahara", characterized by steppe, savanna, and shrub vegetation, and fewer deserts than today (Dallmeyer et al., 2020; Hoelzmann et al., 1998; Jolly et al., 1998). Such vegetation is required to sustain the enhancement and northward extent of the WAM during the MH. The simulation with ECHAM5-wiso used MH vegetation patterns provided by the BIOME6000 vegetation reconstructions (Bigelow et al., 2003; Harrison et al., 2001; Pickett et al., 2004; Prentice et al., 2000), where the Sahara desert was drastically reduced, and the Sahelian vegetation belt, consisting of steppe, tropical dry forest, and xerophytic woods/shrubs, was extended northward (Jolly et al., 1998; Prentice et al., 2000). Through positive feedback, vegetation has been suggested to increase orbitally driven precipitation across North Africa due to the warming effect caused by reduced albedo (Bonfils et al., 2001) and increased evapotranspiration as a result of increased latent heat fluxes (Levis et al., 2004; Texier et al., 2000). Overall, moisture recycling through evapotranspiration and induced surface warming increases convection and inland moisture flux and intensifies the WAM. However, previous studies have also indicated a plausible negative vegetation feedback on precipitation at the annual scale due to a larger contribution of soil evaporation than the albedo feedback under wetter conditions (Notaro et al., 2008; Y. Wang et al., 2008).
2. The lower values of greenhouse gas (GHG) concentrations used for the PMIP4-CMIP6 MH experiments. Lower pCO_2 would result in a slightly colder climate than that produced by the ECHAM5-wiso simulation. This has been shown for the PMIP3-CMIP5 MH experiments that used GHG concentrations that are similar to those used for our ECHAM5-wiso experiment. The differences between PMIP4-CMIP6 and PMIP3-CMIP5 were due to the simulated difference in effective radiative forcing of -0.3 Wm^{-2} (Otto-Bliesner et al., 2017). Generally, the slightly colder climate would reduce the temperature meridional gradient across the African continent that drives low-level south-westerly moist air masses from the equatorial Atlantic Ocean.
3. The use of the high spatial resolution for the ECHAM5-wiso simulation. Several studies have demonstrated that monsoons are better resolved when resolution is increased, even though the magnitude changes are more susceptible to the model's parameterization (e.g., Gao et al., 2006; Sperber et al., 1994). The higher spatial resolution consequently reproduces the MH patterns through improved representation of important processes, such as large-scale condensation, land-sea interaction, and topographic forcings (Boyle & Klein, 2010). Bosmans et al. (2012) showed that using a high-resolution (T159) for EC-Earth GCM resulted in an increased intensity and a greater northward reach of the WAM in the MH when compared to the low-resolution PMIP2 ocean-atmosphere coupled models. The inter-model variabilities can also be attributed to the differences in complexities and the models' sensitivity to the parameterization of clouds, atmospheric dynamics, and the hydrological cycle in general. We highlight that determining the influence of resolution and model parameterization is beyond the scope of this manuscript. Overall, all the models estimate similar latitudinal precipitation patterns across the WAM region, but the predicted northward reach and regional precipitation amounts are too low to sustain the plant types that exited during the MH (Braconnot et al., 2007; Joussaume et al., 1999).

5.1.2. Last Glacial Maximum (~21 ka)

Generally, the global climate during the LGM was characterized by large-scale cooling due to radiative perturbations linked to the extensive continental ice sheets and lower atmospheric greenhouse gas (GHG) concentrations (Clark et al., 2009). These large-scale drivers were further modified by internal feedbacks in the climate system involving factors like sea ice, snow, and water vapor (e.g., Braconnot et al., 2007). ECHAM5-wiso simulates realistic patterns of temperature anomalies, indicating maximum cooling of approximately -15°C across regions with ice sheets in the Northern Hemisphere, and moderate cooling (-2 to -5°C) over tropical areas (Figure S9 in Supporting Information S1). These patterns are similar to the results of PMIP4-CMIP6 experiments and align with findings from previous modeling studies (e.g., Cao et al., 2019; Kageyama et al., 2021). The large perturbations in the atmospheric radiative balance due to albedo feedbacks also result in significant changes in atmospheric circulation patterns, contributing to comprehensive changes in precipitation patterns (e.g., Liakka et al., 2016; Liakka & Lofverstrom, 2018). Large ice sheets covering North America and Fennoscandia redirect

low-level winds, which strongly influences moisture transport and regional precipitation. Additionally, the associated thermodynamics, as indicated through specific humidity, can contribute to regional precipitation changes (D'Agostino et al., 2019, 2020). Most of the precipitation on land was substantially decreased due to the large-scale cooling and its associated reduction in evapotranspiration (e.g., Braconnot et al., 2007). The lower SSTs led to reduced evaporation over the oceans, which in turn reduced the surface's moisture flux into the atmosphere. This eventually led to a decreased inland moisture flux, leading to overall large-scale drying. Apart from surface cooling, tropospheric cooling also decreased the amount of atmospheric water vapor by limiting its water-holding capacity through the Clausius-Clapeyron relation. However, in both hemispheres, other regions across the mid-latitudes experienced an increase in precipitation, mainly in areas corresponding to the positions of the North Pacific, North Atlantic, and Southern Ocean storm tracks (Figure S9 in Supporting Information S1). The simulated temperature patterns indicate overall cooling across the African continent, suggesting that the meridional temperature and pressure gradient that drives northward moisture flux from the Atlantic Ocean are suppressed, thereby reducing moisture availability across the WAM areas. Furthermore, the surface cooling over the oceans was more intense than over land, indicating a decrease in the land-sea thermal contrast, which would result in an additional reduction in inland moisture transport.

5.1.3. Mid-Pliocene (~3 Ma)

Simulating the MP climate provides the opportunity to evaluate the long-term response of the climate system to currently raised atmospheric GHG concentrations. This period is often considered an analog for future climate change (Burke et al., 2018) due to its similarities to modern paleogeography and high pCO_2 (400 ppm). As such, the modeling framework of the MP helps assess how important climatic components of the Earth system, such as the El Niño-Southern Oscillation, the global hydrological cycle and monsoon systems, respond to the ongoing rise in CO_2 concentrations. The simulated temperature patterns predict a global mean near-surface temperature increase of approximately 3°C, primarily due to direct CO_2 forcing. The overall warming exhibits polar amplification, with temperature anomalies increasing by more than 10°C due to associated changes in albedo at higher latitudes (Chandan & Peltier, 2020; de Nooijer et al., 2020; Samakinwa et al., 2020; Tindall et al., 2022). The simulated global mean temperature increase predicted by ECHAM5-wiso falls within the range of model estimates (1.4–4.6°C) from the PlioMIP Phase 1 and 2 experiments (Haywood et al., 2013, 2020). The significant warming in high latitudes reduces the meridional temperature gradient, weakening the tropical atmospheric circulation, specifically the Hadley circulation (Corvec & Fletcher, 2017; Haywood et al., 2013). Previous studies also indicated a poleward shift of mid-latitude westerly winds (Li et al., 2015), increased intensity of tropical cyclones (Yan et al., 2016), and strengthening and poleward extension of the global land monsoon system (Li et al., 2018). The enhanced hydrological cycle intensifies the East Asian and West African summer monsoons (R. Zhang et al., 2013, 2016). These changes resemble future climate projections (e.g., Erfanian et al., 2016; Seth et al., 2019) and require detailed understanding from a modeling perspective.

Through sensitivity experiments, (Stepanek et al. (2020) determined that MP paleogeography contributes to increased rainfall across the WAM areas. The closure of the Arctic gateway and enhanced topography have also been suggested to strengthen the Atlantic Meridional Overturning Circulation (AMOC), thereby warming the North Atlantic Ocean (Z. Zhang et al., 2021), which impacts the WAM (Mulitza et al., 2008). These findings highlight the importance of other boundary conditions in regulating the WAM. As mentioned earlier, land surface conditions, such as vegetation, contribute to the variability and spatial extent of the WAM through evaporative fluxes. Proxy reconstructions from previous studies suggest more humid conditions across northern Africa, which facilitates an expansion of vegetation. More specifically, palynological records suggest high tree cover density and broadening of woodlands and savannas at the expense of deserts across the Sahara (Bonnefille, 2010; Salzmann et al., 2008). ECHAM5-wiso was set up with converted PRISM3 vegetation reconstructions, which indicate the expansion of grass and forests across North Africa toward the Mediterranean (Figure S10 in Supporting Information S1). Such patterns are also consistent with the COSMOS dynamic vegetation results presented in Stepanek et al. (2020), which estimated an increase in precipitation by 70 mm/month across the WAM region. The PlioMIP2 models with prescribed MP vegetation also indicate a strengthened WAM, with an ensemble mean of precipitation showing an increase by ~76 (60–120) mm/month (Berntell et al., 2021). The previous modeling inter-comparison project (i.e., PlioMIP1) estimates a lower magnitude of increase within a range of 30–60 mm/month (R. Zhang et al., 2016). The PlioMIP1 experimental protocol (Haywood et al., 2010) was similar to the model setup used for the ECHAM5-wiso simulation. These findings suggest that ECHAM5-

wiso simulates a higher magnitude of WAM precipitation in the MP than the PlioMIP1 models. This may be due to the higher spatial resolution used for ECHAM5-wiso, which improves representation of land surface conditions (e.g., orography and vegetation) and model parameterization. Overall, PlioMIP1 and PlioMIP2 models suggest that the updated MP boundary conditions from PRISM3 to PRISM4 contribute to the strengthening of the WAM. Samakinwa et al. (2020) confirm this with a sensitivity experiment using COSMOS, which indicated that the updated paleogeography was the main reason for the changes in the large-scale features between PlioMIP1 and PlioMIP2.

The precipitation simulated with ECHAM5-wiso shows an increase of up to 120 mm/month and an intensification toward the east (Figure 3). However, regional means of precipitation across the Sahel increase by only ∼50 mm/month, which falls within the broader range of PMIP4-CMIP6 estimates (10–160 mm/month) (Figure 4). The CESM2 and EC-Earth3-LR models estimate significant increases of 90 and 160 mm/month, respectively. The HadGEM3-GC31-LL, IPSL-CM6A-LR, and NorESM1-F estimate a moderate increase of ∼50 mm/month, with GISS-E2-G estimating the lowest increase of only ∼10 mm/month. The magnitude of the precipitation response simulated by the individual models across the WAM is consistent with the global response. For instance, GISS-E2-1-G indicates a low global response to the MP boundary conditions and consistently estimates the lowest WAM precipitation anomalies. On the contrary, models with large land-sea rainfall anomalies (e.g., EC-Earth3-LR and CESM2) also simulate a strengthened WAM. Even though the updated boundary conditions contributed to the inter-model variabilities, Haywood et al. (2020) suggested model parameterization and initial conditions as the main factors for the varied predictions. Moreover, later model versions tend to have a higher sensitivity than earlier versions when used with the same boundary and initial conditions. These findings suggest that using ECHAM6-wiso (Cauquoin et al., 2019) and even updated PRISM4 reconstructions (Dowsett et al., 2016; Haywood et al., 2016) would increase the strengthening of the WAM in the model.

5.2. Control of the Precipitation and Temperature on Stable Oxygen Isotope in the WAM Season in Response to the Different Past Climates

The stable oxygen isotopic composition of tropical precipitation provides information about the hydrological cycle and can be used to reconstruct past tropical climates. Several studies have employed stable isotopes to understand the intraseasonal water cycle variability in western Africa (e.g., Risi et al., 2008, 2010). These studies have revealed that the integrated convective activity in the monsoon season is spatially and temporally reflected in the $\delta^{18}O$ values in precipitation and vapor records. On a broader scale, previous studies have used isotopic patterns to identify the strengthening of the Northern Hemisphere monsoon in response to warmer climates, both through modeling (e.g., Cauquoin et al., 2019; Shi et al., 2023; Thompson et al., 2021) and proxy records (Bartlein et al., 2011; Wang et al., 2008). Simulating the isotopic composition allows for a direct comparison of model simulations to isotopic archives and contributes to the understanding of the causal mechanisms behind various proxy archives (Bühler et al., 2022; Phipps et al., 2013; Risi et al., 2012; Werner et al., 2000). Here, we explore the response of simulated $\delta^{18}O_p$ to varied paleoenvironmental conditions during the WAM season. The results suggest that meteoric water was more negative in past warmer climates and less negative in colder climates. Similar patterns have been reported in previous isotope-enabled GCM modeling studies (e.g., Cauquoin et al., 2019; Risi et al., 2010). Specifically, the oxygen isotopes are most depleted during the MH, indicating the role of seasonal insolation distribution and associated precipitation dynamics in the isotopic patterns (Thompson et al., 2021). Importantly, the magnitude and spatial patterns, to some extent, are inconsistent with the simulated precipitation anomalies despite the expected dependence of the isotopic composition on convective activity, as suggested in previous studies (e.g., Bony et al., 2008; Lawrence et al., 2004). These changes reveal the plausibility of additional factors controlling $\delta^{18}O_p$ in different climates. Therefore, we further explore the relative influence of precipitation and temperature on the simulated $\delta^{18}O_p$ patterns to better understand what controls the oxygen isotopes during the monsoon season.

We evaluate the control of precipitation and temperature on $\delta^{18}O_p$ values in different time periods by calculating their linear relationship during the WAM season using Spearman correlation analysis. The PI simulation yields north-south bidirectional correlation patterns between precipitation and $\delta^{18}O_p$ values, with significant negative correlations (≥ -0.8) over the Guinea Coast up to the Sahel (0–15°N) and positive correlations (≥ 0.7) across the Sahara (Figure 12). The strong negative relationship along the coastal region toward the Sahel indicates the amount effect, as is expected based on previous studies (Lawrence et al., 2004; Rozanski et al., 1993). Convective activity has been well established as the main factor driving the spatial and temporal patterns of the isotopic

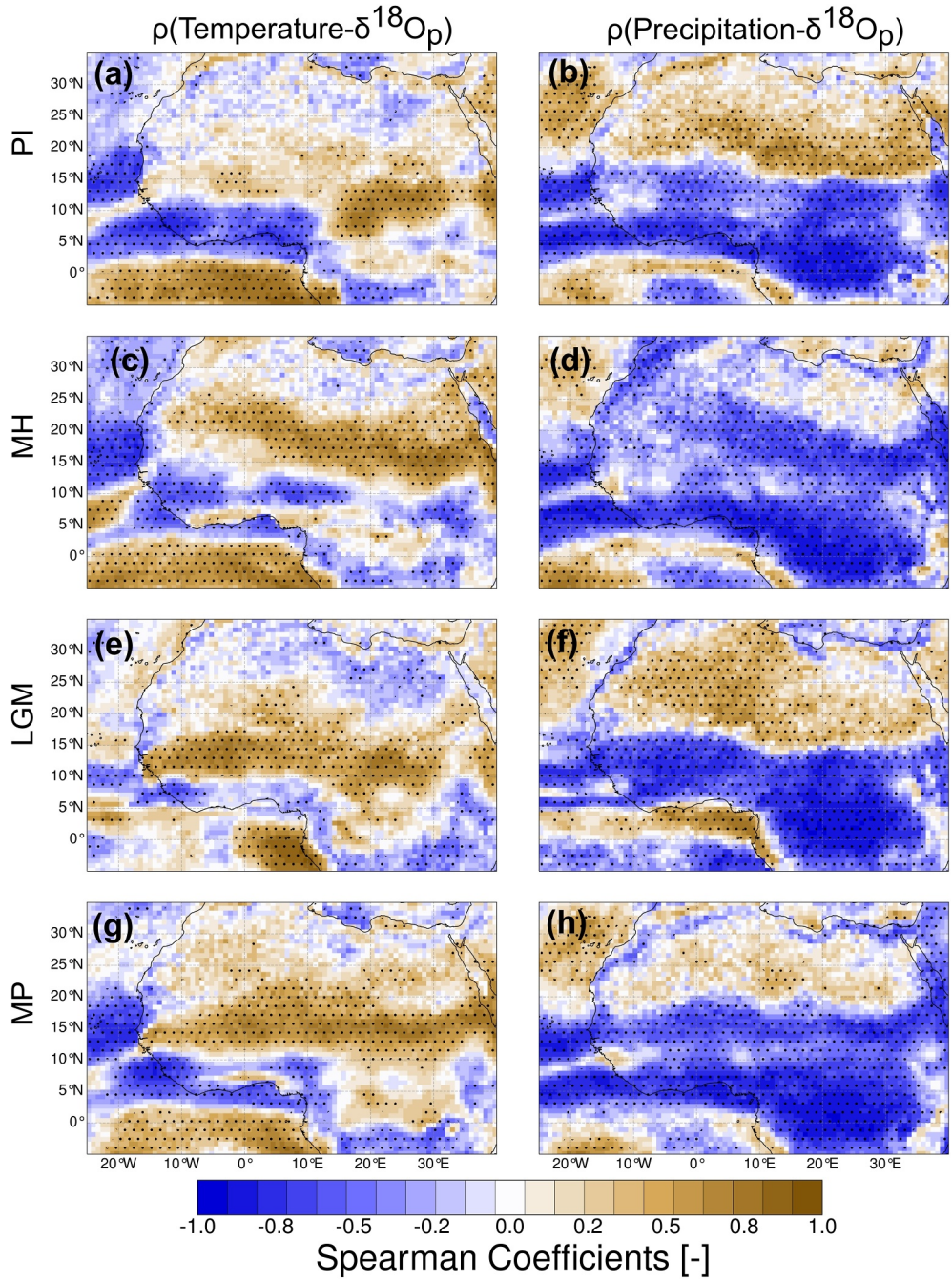

Figure 12. Spearman correlation coefficients for the interannual relationship between the simulated monthly means of $\delta^{18}O_p$ and precipitation amount (right panel) and temperature (left panel) during the WAM months (JJAS). The dot stippling represents the regions with significant correlation coefficients with a 95% confidence interval. The correlations' magnitude and spatial patterns are not stationary in response to the different climates. For example, the bi-directional north-south $\delta^{18}O_p$-precipitation relation transitions to an overall negative relationship in the Mid-Holocene (MH).

composition of precipitation and vapor (Bony et al., 2008; Lawrence et al., 2004; Risi et al., 2008). The reasons why an increase in precipitation amount results in the depletion of the heavy oxygen isotope across the WAM might be partially due to the fact that (a) the increase in rainfall amount moistens the atmosphere, which reduces rainfall re-evaporation and diffusive fluxes, and ultimately results in lower $\delta^{18}O_p$ values in raindrops; (b) intense convective activity increases vertical mixing in the form of unsaturated downdrafts, so that the associated depletion of low-level vapor feeds into subsequent convective systems with lower $\delta^{18}O_p$ values (Lawrence

et al., 2004; Risi et al., 2008). The change in correlation direction over the Sahara indicates that the "amount effect" is limited across the Sahel region, where the maximum rain belt is situated during the monsoon season. These changes are unsurprising, as the rainout of the moisture transported from the equatorial Atlantic Ocean would deplete the remaining air masses of heavy oxygen isotopes. However, during the retreat of the WAM, evaporative recycling provides a moist air mass with relatively enriched heavy oxygen isotopes that condense to rainfall. These changes suggest the influence of continental recycling on the isotopic patterns across the Sahel. Surface evaporative fluxes through continental recycling result in air masses that are less negative than oceanic fluxes (Risi et al., 2013). Moreover, the warmer and drier conditions across the Sahara would contribute to more re-evaporation of falling vapor, leading to an enrichment in the heavier isotope in relation to the source (Risi et al., 2008). The LGM and MP simulations indicate similar correlation dipole patterns across the WAM, but the positive relationship across the Sahara in the MP is less significant (Figure 12). Nevertheless, the correlation patterns in the MH indicate an overall negative link across the whole WAM region, suggesting that the amount effect predominantly controls the oxygen isotopic patterns. The changes in the correlation structure across different past climates suggest the non-stationarity of the controlling mechanism across the WAM areas.

The correlation analyses for $\delta^{18}O_p$ and temperature yield fewer regions with significant correlation due to the predominant influence of precipitation amount on $\delta^{18}O_p$ during the WAM season. The analysis indicates positive correlation patterns over the Sahara, which extends further northward in the MP. The expanded area of positive correlation in the MP highlights the importance of continental recycling during the retreat of the WAM. These patterns also validate the wider spread of precipitation during the retreat months in the MP (Figure 6d), which has also been suggested in previous studies (Berntell et al., 2021). We highlight that the estimated interannual relationships from the simulated paleoclimate time slices only serve as a surrogate to evaluate the non-stationarity of the relationship between the $\delta^{18}O_p$ and surface climate variables and do not necessarily reflect the causal mechanisms of the interannual variability of the proxy record. Although this analysis is limited to empirical evidence that does not consider causal mechanisms, the results clearly indicate that proxy reconstructions must efficiently understand the regional climatic influence on various proxy records. This would help resolve the inaccuracies in paleoclimate and paleoenvironment reconstructions that assume the stationarity of the calibrated transfer function (e.g., Kolstad & Screen, 2019; Raible et al., 2014). The comparison of the simulated isotopic values to proxy records and the investigation of the causal mechanisms leading to the available proxy records is beyond the scope of this study.

5.3. Atmospheric Dynamics Driving the Simulated WAM Changes

Overall, the response of the WAM to GHG forcing, vegetation changes, and orbital forcing is mostly associated with the changing meridional temperature gradient. A more pronounced gradient drives the increased intensity and higher altitude reach of the low-level southwesterlies and a more northward position of the ITD and AEJ. On the other hand, the weakening of the WAM in response to colder conditions can be attributed to the weak or non-existent meridional temperature and pressure gradient. This less pronounced gradient would lead to moisture transport into the continent and into the troposphere to suppress the wind shear of the AEJ. We discuss these simulated dynamics in the context of what has been suggested in previous studies, while also highlighting the new findings.

The pronounced summer meridional temperature and pressure patterns in the MH and MP climates are consistent with the PMIP4 model results (e.g., Berntell et al., 2021; Brierley et al., 2020; Kageyama et al., 2021). These temperature anomalies reflect the patterns of increased precipitation, namely wetter conditions across the Sahel to coastal regions in the MH and MP. The warming over the high latitudes deepened the Sahara Heat Low, inducing low-level moisture convergence and strengthening the south-westerly flow that transports moisture from the equatorial Atlantic into the continent (Lavaysse et al., 2009). In the MH, the warming across the Sahara and the cooling over the Sahel are more intense than in the MP. The increased insolation across the Northern Hemisphere was the main driver of the intense warming across the Sahara. On the other hand, the cooling over the Sahel is partly due to the cloudiness associated with increased precipitation due to enhanced moisture flux into the Sahel areas. Another factor may be the increased evaporative fraction (Figure S8 in Supporting Information S1) and upward latent heat flux (Figure 11), which moisten the soil and reduce the energy available to heat the near-surface air through sensible heat flux. These mechanisms (a) cool the surface where precipitation increases and (b) further strengthen the north-south gradient to drive moisture advection into the WAM region. This feedback indicates that moisture advection strengthens the WAM more than local recycling does (Marzin &

Braconnot, 2009; Y. Zhao et al., 2005). However, the internal feedback reinforces the pressure gradient and determines the northward migration of the WAM through evaporative recycling. In the MP, the seasonal precipitation distribution indicates a delayed WAM retreat with more precipitation during the southward retreat months than in the MH. Such precipitation seasonality highlights the role of internal feedback since the evaporative recycling supplies more moisture during the retreat months. Furthermore, cooling across the Sahel in the MP is more significant toward the east. These patterns coincide with the relative increase in upward latent heat flux toward the east, suggesting more moisture availability through local feedback to strengthen the cooling (Figure 11). Even though the MP has higher atmospheric CO_2 with an enhanced hydrological cycle, this study reveals that the orbital forcing and expanded vegetation in the MH produces the highest intensity of the WAM. These imply that GCMs must adequately represent these features to ensure accurate projections of the WAM in response to future climate change. In the LGM climate, the overall cooling and drying conditions prevent the initiation of a meridional pressure gradient to drive moisture into the continent. This resulted in continuous wind patterns from the Tropical Atlantic into the North Atlantic Ocean without diverging into the continent, as suggested in previous studies (e.g., Jiang et al., 2015; Kageyama et al., 2021; Otto-Bliesner et al., 2006). Overall, the strengthening of the meridional temperature and pressure gradient determines the intensity of the southwesterlies, northward migration of the WAM, and its altitudinal reach, which affects the location of the ITD and AEJ.

The simulated intensity and location of the AEJ and its relationship to the strengthening of the WAM suggest a complex causal mechanism. More specifically, the simulated core of the AEJ is situated at higher latitudes (15–20°N) and altitudes (600–500 hPa) in summer during the MH and MP than in the PI and LGM. These patterns are not surprising since the strengthened WAM in these climates is associated with a more northward position of the ITD and deeper monsoon depth (Janicot et al., 2011; Nicholson, 2009). Moreover, the surface temperature gradient maintains the AEJ, along with two meridional circulations forced by the dry convection of the Sahara Heat Low to the north and the moist convection driven by the ITCZ to the south (Thorncroft & Blackburn, 1999; Wu et al., 2009). Usually, the monsoonal flow of the low-level southwesterlies reaches far into the mid-troposphere to weaken the shear of the AEJ and shift it to higher latitudes (Patricola & Cook, 2007; Texier et al., 2000). However, the simulated intense monsoonal flow due to the pronounced meridional temperature gradient in the MH induces high AEJ intensity when compared to the MP. On the other hand, the reduced monsoonal flow simulated in the LGM also results in an AEJ intensity that is higher than PI. These causal relationship patterns indicate that the weakening of the AEJ is not entirely associated with the strengthening of the WAM, especially when orbital forcings mainly control large-scale climatic features. Therefore, the atmospheric dynamics response simulated in this study confirms that the position of the AEJ is more important in strengthening the WAM than its intensity, as suggested in previous studies (Jenkins et al., 2005; Nicholson, 2008; Nicholson & Grist, 2001; Nicholson & Webster, 2007). These suggest that the intensity of the AEJ is an effect rather than a cause (Newell & Kidson, 1984). The complexity of the causal relationship between AEJ and Sahel rainfall and its varied feedback, as reported by some studies, might be due to its sensitivity to localised conditions, which is represented differently in GCMs. For instance, Texier et al., 2000; Patricola & Cook, 2007 reveal that the decrease or even disappearance of the AEJ is achieved when the GCM is coupled to a dynamic vegetation model. Contrarily, Texier et al., 2000 produced an increased AEJ located further north without dynamic vegetation feedback in the model.

The simulated TEJ intensity shows consistent patterns of increasing shear due to wetter conditions, as indicated by previous studies (e.g., Nicholson and Klotter 2021). The simulated intensity in the MH and MP revealed no significant changes, but was higher than LGM and PI (Figure 10). The TEJ is mostly driven by large-scale remote features such as convective heating over the North Indian Ocean and the Himalayan-Tibetan plateau (Gill, 1980). However, Redelsperger et al. (2002) indicate that the latent heat release through convection over the WAM can enhance upper-level shear, thereby intensifying the TEJ. The causal mechanisms through which the intensified TEJ increases the Sahel rainfall have been proposed in many studies (Lemburg et al., 2019). These include upper-level divergence (Nicholson & Grist, 2003), vertical and horizontal shear and how it affects dynamic instabilities (Grist, 2002; Nicholson, 2008), and the modulation of the equatorial Rossby wave activity (Yang et al., 2018).

The results reveal both the localised and large-scale impacts of vegetation on precipitation over the WAM areas in response to different climates. Generally, vegetation influences the exchange of mass and energy between the land surface and the atmosphere through the modulation of (a) surface albedo, influencing surface radiation, and (b) evapotranspiration, influencing the partitioning of net radiation into surface heat fluxes. These imply that land cover does not only affect surface climate but also influences atmospheric convection and large-scale circulations

and moisture fluxes, which create further feedback and influence soil moisture and vegetation (Charney et al., 1977; Sylla et al., 2016). In this study, we focus on analyzing the influence of surface conditions through surface heat flux anomalies. Previous modelling studies have highlighted the role of soil moisture and evapotranspiration in the vegetation-precipitation feedback due to their effect on low-level moist static energy, convective instability, and surface latent heat flux anomalies (Patricola & Cook, 2007; Rachmayani et al., 2015). These feedback mechanisms have been shown to strengthen the response of the WAM to external forcing in past warmer climates (e.g., Messori et al., 2019). The expanded vegetation over the Sahara in the MH resulted in a pronounced upward latent heat flux, further strengthening the WAM and the moisture influx through the vegetation-albedo feedback (e.g., Bonfils et al., 2001; Levis et al., 2004). The less expanded vegetation in the MP also strengthened the WAM and contributed to the increased precipitation in the retreat months of the WAM, even though the meridional pressure gradient was weaker than in the MH. Previous studies have indicated wetter conditions and a northward migration of the WAM that is driven by the cyclonic moisture flux anomaly over North Africa due to expanded vegetation into the Sahara region (Chandan & Peltier, 2020; Pausata et al., 2020; Swann et al., 2014). Since the various atmospheric dynamics and surface conditions had a unidirectional influence on the WAM, isolating the impact of vegetation, a local amplifier forced by other large-scale features (e.g., Klein et al., 2017; Messori et al., 2019), would require further sensitivity experiments.

5.4. Comparison of Model Estimates to Proxies

Comparing modeled paleoclimate to proxy reconstructions over Africa is often challenging, because of the varying representation of relevant atmospheric processes in different GCMs, and high spatial variability of proxy signals (e.g., deMenocal et al., 2000; Harrison et al., 2014; Hopcroft & Valdes, 2019; Pausata et al., 2016; Tierney et al., 2017). Moreover, the relatively low availability of paleohydrological records over Africa precludes a robust model-data comparison (e.g., Salzmann et al., 2008, 2013). The sparsity of proxies also prevents the merited direct comparison of simulated isotopic composition with past isotopic archives. Here, we focus on the MH model-data comparison due to the relatively large number of proxy reconstructions available (Figure S12a in Supporting Information S1) and the ongoing debate about the northward migration and intensification of the WAM during the African Humid Period (e.g., Pausata et al., 2020). The sparse tropical African proxy records for the LGM reported in previous studies have shown consistent cooling and drying conditions (Figure S12b in Supporting Information S1; Bartlein et al., 2011). It has been suggested that the dryness induced a downward elevational shift of broadleaved evergreen or warm mixed forest and the enrichment of steppe into regions now occupied by tropical forests (e.g., Elenga et al., 2000). The reconstructed proxy records over North Africa during the MP consistently suggested more humid conditions (Figure S12c in Supporting Information S1; Feng et al., 2022). More specifically, palynological data reveals denser tree cover and expanded woodland and savanna at the expense of deserts over North Africa (Bonnefille, 2010; Salzmann et al., 2008). Such vegetation expansion patterns are consistent with the only dynamic vegetation GCM output participating in PlioMIP2 (Stepanek et al., 2020). Moreover, multi-proxy records, including plant wax and dust from marine sediment cores from offshore West Africa (Figure S12c in Supporting Information S1), suggest consistent wetter conditions in the MP (deMenocal, 2004; Feng et al., 2022; Kuechler et al., 2018). These reconstructed patterns are consistent with the more humid and dryness simulated for the LGM and MP in this study.

In the remainder of this section, we compare the simulated latitudinal variation of Mean Annual Precipitation (MAP) during the MH to pollen-based reconstructions by Bartlein et al. (2011) and leaf wax isotope-based reconstruction by Tierney et al. (2017). Overall, the simulated MAP magnitudes and latitudinal distribution by ECHAM5-wiso are closer to the proxy reconstructions than the PMIP4 models (Figure 13). More specifically, the ECHAM5-wiso inter-annual means of the WAM's northward extent compare well to the lower latitudes of the proxy data over the Sahara with regards to the magnitude of changes and the patterns from the Sahel towards the tropical ocean. However, all models (i.e., PMIP4 models and ECHAM5-wiso) failed to match the magnitudes of the proxy-based MAP increase over the high latitudes of the Sahara. The simulated MAP increase over the Sahara was 100–300 mm/year less than the proxy reconstruction. It is important to note that the calculated MAP anomalies of the pollen-inferred precipitation proxy records used present-day CRU observation data as a reference period, while the GCMs used their PI simulations. Although the different reference periods can contribute slightly to the discrepancies, the magnitude of the difference is large enough to acknowledge significant deviations and thus potential limitations of either the GCMs or the proxy-based reconstructions. The simulated ECHAM5-wiso anomalies during the monsoon season indicated wetter conditions up to 25°N, with increased

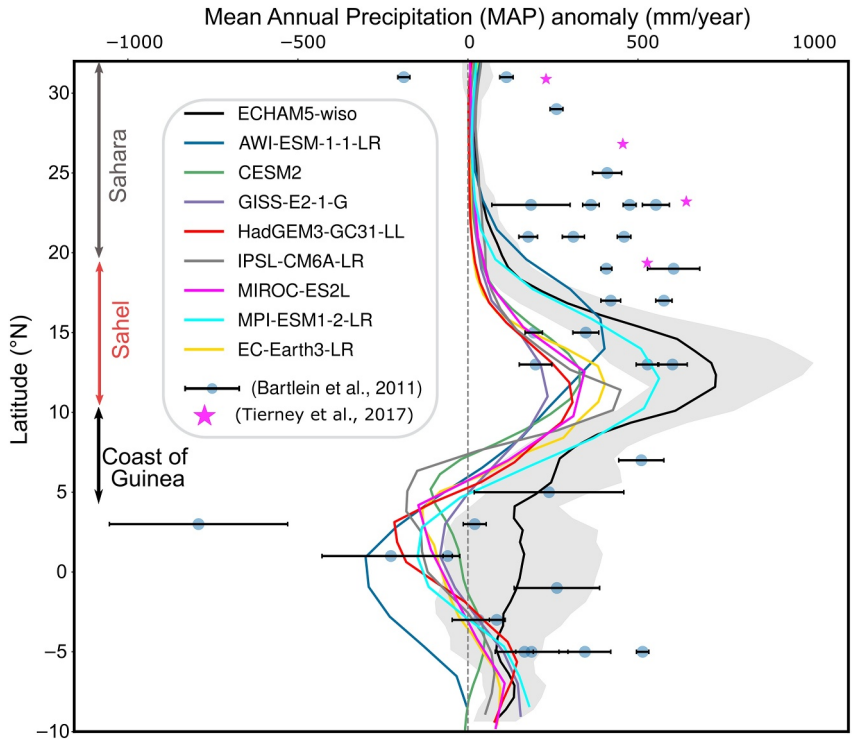

Figure 13. Comparison of the mean annual precipitation (MAP) anomalies of the latitudinal extent of WAM in the Mid-Holocene for all models (ECHAM5-wiso (black) and PMIP4 models) to pollen-inferred (Bartlein et al., 2011; blue circles) and leaf wax-inferred (Tierney et al., 2017; magenta stars) precipitation reconstruction. The black shadings denote one standard deviation value from the regional means of the ECHAM5-wiso simulation. The error bars of the proxies represent the standard errors of the precipitation reconstructions.

precipitation anomalies of approximately 700 mm/year (Figure 3). This suggests a potential overestimation of precipitation anomalies from the pollen-based records on the annual scale due to their potentially biased representation of the dry seasons across the Sahara. In addition to the pollen-based reconstructions, other diverse archives over West Africa estimate precipitation differences in the range of 300–500 mm/month, which are within the range of our model estimates (Harrison et al., 2014; Kröpelin et al., 2008; Tierney et al., 2017). On the other hand, recent reconstructions of leaf wax-alkane records off the coast of northern Africa suggest MAP increase of up to 600 mm/year (compared to PI) as far north as 31°N (Figure 13), implying an expansion of the WAM in the MH to 15–20° north of its present-day extent (Sultan & Janicot, 2003; Tierney et al., 2017). Sha et al. (2019) interpreted their Moroccan speleothem at 31°N with high negative $\delta^{18}O$ of carbonate records as a high rainfall signal created by the expansion of the WAM during the MH. Paleoenvironment reconstructions also reflect wetter conditions in the MH with higher lake levels and moisture-demanding biomes across North Africa (Kohfeld & Harrison, 2000; Peyron et al., 2006; H. Wu et al., 2007). Vegetation reconstructions suggest a northward shift of montane forest and a major extension of the tropical rainforest over North Africa (Jolly et al., 1998; Prentice et al., 2000).

Overall, the model-proxy comparison reveals that all the adopted GCMs show limited skill in reproducing the northward migration of the WAM and associated rainfall increase over the Sahara. This suggests that the shortcomings leading to these discrepancies are shared by all models and are not GCM-specific. The WAM dynamics are sensitive to the representation of climate physics in the GCMs. Their limitations include inaccuracies in representing clouds, surface conditions (e.g., lakes and wetlands), energy fluxes, and subgrid-scale convection parameterisation. Additionally, the coarse spatial resolution of GCMs weakens their ability to reproduce the mesoscale convection systems that are the main driver for the WAM. Previous studies have also indicated that fully coupled models exhibit biases in reproducing the tropical Atlantic dynamics, leading to elevated sea surface temperatures and a weakened monsoonal circulation (Roehring et al., 2013). In this study, the high spatial resolution of the ECHAM5-wiso experiment contributed to a better representation of surface

conditions, such as orography. Furthermore, the model was prescribed MH vegetation reconstruction. Contrarily, the PMIP4 models are fully coupled (atmosphere-ocean), incorporating ocean variability feedback, and some consider dynamic vegetation feedback. Since all models, that is, both ECHAM5-wiso and the PMIP models, exhibit the above-mentioned deviations from proxy reconstructions, we propose that the limitations are neither related solely to spatial resolution nor the use of fully coupled models. Harrison et al. (2015) suggests the simulated biases of the PI control experiments of the PMIP4-CMIP6, which indicate a more equatorward ensemble mean of the global monsoon when compared to observations. Previous models have also shown that atmosphere-vegetation feedback contributes to the northward extent of the WAM, but still underestimates the higher latitude precipitation amount from the leaf wax n-alkanes (Dallmeyer et al., 2020; Pausata et al., 2016; Thompson et al., 2019). Rachmayani et al. (2015) demonstrated that dynamic vegetation enhances the orbitally driven increase in precipitation anomalies over West Africa by 20% when compared to models using fixed vegetation. However, their models with terrestrial and ocean feedback still did not reach the level of vegetation coverage suggested by proxies.

Recent studies have demonstrated that incorporating dust feedbacks associated with the Green Sahara in the MH orbitally driven climate further enhances the northward reach and intensification of the WAM (e.g., Egerer et al., 2018; Hopcroft & Valdes, 2019; Pausata et al., 2016; Thompson et al., 2019) and better matches the paleoclimate reconstructions. This is because the albedo-related feedback causes a reduction of dust concentration and changes in soil properties over the vegetated Sahara, which induce an increase in incoming shortwave radiation on the land surface, strengthening the warming over the Sahara. This further strengthens the meridional temperature gradient and tropical circulation and then intensifies the WAM (Chandan & Peltier, 2020; Pausata et al., 2016). Pausata et al. (2016) demonstrated the northward extent of the WAM up to 31°N in the MH with a model forced with prescribed vegetation and reduced dust concentrations, while the prescribed vegetation only reached ∼26°N. These suggest that simulating vegetation feedback with interactive dust dynamics on a high spatial resolution grid would improve the representation of the MH. However, the state-of-art GCMs would require improvement of their physical representation of dust dynamics, since they fail to reproduce dust emission and transport (Evan et al., 2014; Kok, 2010; Leung et al., 2023; A. Zhao et al., 2022). On the other hand, the plausible non-stationarity of the pollen-precipitation transfer function due to changes in past climate dynamics from present conditions can also contribute to the mismatch between climate simulation and paleoclimate reconstructions. Therefore, using a multi-proxy system with varied causal mechanisms could ensure an accurate representation of the WAM complex dynamics.

6. Conclusions

This study presents new and existing climate model simulations of the WAM and associated features in the Late Cenozoic (i.e., the PI, MH, LGM and MP). More specifically, the study presents an overview of the hydroclimate changes over West Africa and highlights the components of the regional climate system that are important for generating accurate projections of future climate. The paleoclimate experiments were conducted using the isotope-tracking model (ECHAM5-wiso). The simulated results are similar to the CMIP6-PMIP4 experiments and proxy reconstructions over West Africa. However, our simulations also show some improvement over previous experiments, and yield new insights. We summarize the key results as follows:

1. A comparison between the present-day ECHAM5-wiso simulation and observation-based data sets (i.e., ERA5 and CRU precipitation and temperature data sets) demonstrates the model's ability to represent the atmospheric dynamics over West Africa reasonably well.
2. The ECHAM5-wiso paleoclimate simulations produce the most intense WAM during the MH, despite the MP's more enhanced hydrological cycle. In comparison, some of the CMIP6-PMIP4 models suggest the highest intensification of the WAM in the MH (e.g., GISS-E2-1-G), while others suggest the MP (e.g., EC-Earth3-LR).
3. The intensification of the WAM is associated with a pronounced meridional gradient, northward position of the ITD, northward reach of the core of the AEJ, higher altitudinal reach of the WAM (deeper monsoon depth), and higher moisture recycling through surface heat fluxes due to vegetation across the Sahel-Sahara region. Most importantly, the AEJ is not entirely responsible for the strengthening of the WAM, especially when large-scale features are predominantly controlled by orbital forcings, as is the case in the MH. This needs to be well-represented in GCMs to ensure realistic and accurate future projections.

4. The simulation of the patterns and magnitude of $\delta^{18}O_p$ values and associated regional climate elements (e.g., temperature and precipitation) during the monsoon season reveal a non-stationarity of their relationship throughout the late Cenozoic. Their changing relationships stress the need to understand the causal mechanisms for each proxy system and refine their transfer function to ensure accurate proxy-based reconstructions.
5. ECHAM5-wiso simulates the higher precipitation rates over the WAM region in the MH than the CMIP6-PMIP4 models. Since our model uses a more accurate vegetation reconstruction and a higher resolution, we propose that a greater consideration of vegetation feedbacks, and sub-grid processes will increase other models' representation of West African climate during the MH.
6. All models still underestimate the northward extent of the WAM, as reconstructed with proxies. If proxy reconstructions are taken as accurate, this suggests that the representation of additional climate processes, such as dust loading, interactive vegetation, and surface conditions, such as lakes, will have to be improved to ensure a more realistic prediction of the WAM's northward extent.

Data Availability Statement

The postprocessed model output variables required to reproduce the figures of this study are available in NetCDF format at https://doi.org/10.5281/zenodo.10455772 (Boateng, 2024). The CMIP6-PMIP4 (Eyring et al., 2016) models output are available at https://esgf-node.llnl.gov/projects/esgf-llnl/ (last access: 03 January 2024). The Climate Research Unit (CRUv4.01) (Harris et al., 2020) precipitation data were obtained from https://crudata.uea.ac.uk/cru/data/hrg/cru_ts_4.01/ (last access: 03 January 2024).

The ERA5 reanalysis products (Hersbach et al., 2020) were obtained from the Copernicus Climate Data Store at https://cds.climate.copernicus.eu/cdsapp#!/home (last access: 03 January 2024).

Code availability statement: The ECHAM model code is available under a version of the MPI-M software license agreement (https://www.mpimet.mpg.de/en/science/models/license/, last access: 03 January 2024). The code of the isotopic version ECHAM5-wiso (Werner et al., 2011) is available upon request on the Alfred Wegner Institute's GitLab repository (https://gitlab.awi.de/mwerner/mpi-esm-wiso, last access: 03 January 2024). The scripts used for postprocessing, analysis, and visualisation are based on a Python package (pyClimat) available at https://doi.org/10.5281/zenodo.7143044 (Boateng, 2022) and also on Github: https://github.com/Dan-Boat/pyClimat (last access: 03 January 2024).

Acknowledgments
This research was supported by the German Science Foundation (DFG) Grants EH329/19-1 and EH329/23-1 (awarded to Todd A. Ehlers), MU4188/3-1 and MU4188/1-1 (awarded to Sebastian G. Mutz). We acknowledge the World Climate Research Programme, which, through its Working Group on Coupled Modelling, coordinated and promoted CMIP6. We thank the climate modelling groups for producing and making their model output available, the Earth System Grid Federation (ESGF) for archiving the data and providing access, and the multiple funding agencies supporting CMIP and ESGF. Additionally, we thank the European Centre for Medium-Range Weather Forecasts for providing ERA5 data sets and the University of East Angelia for producing the CRU data sets. Open Access funding enabled and organized by Projekt DEAL through the University of Tübingen. Open Access funding enabled and organized by Projekt DEAL.

References

Abe-Ouchi, A., Saito, F., Kageyama, M., Braconnot, P., Harrison, S. P., Lambeck, K., et al. (2015). Ice-sheet configuration in the CMIP5/PMIP3 Last Glacial Maximum experiments. *Geoscientific Model Development*, *8*(11), 3621–3637. https://doi.org/10.5194/gmd-8-3621-2015

Adegbie, A. T., Schneider, R. R., Röhl, U., & Wefer, G. (2003). Glacial millennial-scale fluctuations in central African precipitation recorded in terrigenous sediment supply and freshwater signals offshore Cameroon. *Palaeogeography, Palaeoclimatology, Palaeoecology*, *197*(3), 323–333. https://doi.org/10.1016/S0031-0182(03)00474-7

Ait Brahim, Y., Sha, L., Wassenburg, J. A., Azennoud, K., Cheng, H., Cruz, F. W., & Bouchaou, L. (2023). The spatiotemporal extent of the Green Sahara during the last glacial period. *iScience*, *26*(7), 107018. https://doi.org/10.1016/j.isci.2023.107018

Annan, J. D., & Hargreaves, J. C. (2013). A new global reconstruction of temperature changes at the Last Glacial Maximum. *Climate of the Past*, *9*(1), 367–376. https://doi.org/10.5194/cp-9-367-2013

Annan, J. D., & Hargreaves, J. C. (2015). A perspective on model-data surface temperature comparison at the Last Glacial Maximum. *Quaternary Science Reviews*, *107*, 1–10. https://doi.org/10.1016/j.quascirev.2014.09.019

Armitage, S. J., Bristow, C. S., & Drake, N. A. (2015). West African monsoon dynamics inferred from abrupt fluctuations of Lake Mega-Chad. *Proceedings of the National Academy of Sciences*, *112*(28), 8543–8548. https://doi.org/10.1073/pnas.1417655112

Arnold, L., Bréon, F.-M., & Brewer, S. (2009). The Earth as an extrasolar planet: The vegetation spectral signature today and during the last Quaternary climatic extrema. *International Journal of Astrobiology*, *8*(2), 81–94. https://doi.org/10.1017/S1473550409004406

Badger, M. P. S., Schmidt, D. N., Mackensen, A., & Pancost, R. D. (2013). High-resolution alkenone palaeobarometry indicates relatively stable pCO_2 during the Pliocene (3.3–2.8 Ma). *Philosophical Transactions of the Royal Society A: Mathematical, Physical & Engineering Sciences*, *371*(2001), 20130094. https://doi.org/10.1098/rsta.2013.0094

Baidu, M., Schwendike, J., Marsham, J. H., & Bain, C. (2022). Effects of vertical wind shear on intensities of mesoscale convective systems over West and Central Africa. *Atmospheric Science Letters*, *23*(8), e1094. https://doi.org/10.1002/asl.1094

Barbé, L. L., Lebel, T., & Tapsoba, D. (2002). Rainfall variability in West Africa during the years 1950–90. *Journal of Climate*, *15*(2), 187–202. https://doi.org/10.1175/1520-0442(2002)015<0187:RVIWAD>2.0.CO;2

Bartlein, P. J., Harrison, S. P., Brewer, S., Connor, S., Davis, B. A. S., Gajewski, K., et al. (2011). Pollen-based continental climate reconstructions at 6 and 21 ka: A global synthesis. *Climate Dynamics*, *37*(3), 775–802. https://doi.org/10.1007/s00382-010-0904-1

Bartoli, G., Hönisch, B., & Zeebe, R. E. (2011). Atmospheric CO_2 decline during the Pliocene intensification of Northern Hemisphere glaciations. *Paleoceanography*, *26*(4). https://doi.org/10.1029/2010PA002055

Bell, B., Hersbach, H., Simmons, A., Berrisford, P., Dahlgren, P., Horányi, A., et al. (2021). The ERA5 global reanalysis: Preliminary extension to 1950. *Quarterly Journal of the Royal Meteorological Society*, *147*(741), 4186–4227. https://doi.org/10.1002/qj.4174

Bereiter, B., Eggleston, S., Schmitt, J., Nehrbass-Ahles, C., Stocker, T. F., Fischer, H., et al. (2015). Revision of the EPICA Dome C CO_2 record from 800 to 600 kyr before present. *Geophysical Research Letters*, *42*(2), 542–549. https://doi.org/10.1002/2014GL061957

Berntell, E., Zhang, Q., Li, Q., Haywood, A. M., Tindall, J. C., Hunter, S. J., et al. (2021). Mid-Pliocene West African monsoon rainfall as simulated in the PlioMIP2 ensemble. *Climate of the Past*, *17*(4), 1777–1794. https://doi.org/10.5194/cp-17-1777-2021

Biasutti, M. (2013). Forced Sahel rainfall trends in the CMIP5 archive. *Journal of Geophysical Research: Atmospheres*, *118*(4), 1613–1623. https://doi.org/10.1002/jgrd.50206

Bigelow, N. H., Brubaker, L. B., Edwards, M. E., Harrison, S. P., Prentice, I. C., Anderson, P. M., et al. (2003). Climate change and Arctic ecosystems: 1. Vegetation changes North of 55°N between the last glacial maximum, mid-Holocene, and present. *Journal of Geophysical Research*, *108*(D19). https://doi.org/10.1029/2002JD002558

Blunier, T., & Brook, E. J. (2001). Timing of millennial-scale climate change in Antarctica and Greenland during the last glacial period. *Science*, *291*(5501), 109–112. https://doi.org/10.1126/science.291.5501.109

Boateng, D. (2022). A functional based python module for processing, analysis and visualization of climate model output (pyClimat) (Version 0.0.1). [Software]. *Zenodo*. https://doi.org/10.5281/zenodo.7143044

Boateng, D. (2024). West African Monsoon dynamics and its control on the stable oxygen isotopic composition of precipitation in the Late Cenozoic. [Dataset]. *Zenodo*. https://doi.org/10.5281/zenodo.10455772

Boateng, D., Mutz, S. G., Ballian, A., Meijers, M. J. M., Methner, K., Botsyun, S., et al. (2023). The effects of diachronous surface uplift of the European Alps on regional climate and the oxygen isotopic composition of precipitation. *Earth System Dynamics*, *14*(6), 1183–1210. https://doi.org/10.5194/esd-14-1183-2023

Bonfils, C., Noblet-Ducoudré, N., Braconnot, P., & Joussaume, S. (2001). Hot Desert albedo and climate change: Mid-Holocene monsoon in North Africa. *Journal of Climate*, *14*(17), 3724–3737. https://doi.org/10.1175/1520-0442(2001)014<3724:HDAACC>2.0.CO;2

Bonnefille, R. (2010). Cenozoic vegetation, climate changes and hominid evolution in tropical Africa. *Global and Planetary Change*, *72*(4), 390–411. https://doi.org/10.1016/j.gloplacha.2010.01.015

Bony, S., Risi, C., & Vimeux, F. (2008). Influence of convective processes on the isotopic composition (δ18O and δD) of precipitation and water vapor in the tropics: 1. Radiative-Convective equilibrium and tropical ocean–global atmosphere–coupled ocean-atmosphere response experiment (TOGA-COARE) simulations. *Journal of Geophysical Research*, *113*(D19). https://doi.org/10.1029/2008JD009942

Boos, W. R. (2012). Thermodynamic scaling of the hydrological cycle of the Last Glacial Maximum. *Journal of Climate*, *25*(3), 992–1006. https://doi.org/10.1175/JCLI-D-11-00010.1

Bosmans, J. H. C., Drijfhout, S. S., Tuenter, E., Lourens, L. J., Hilgen, F. J., & Weber, S. L. (2012). Monsoonal response to mid-Holocene orbital forcing in a high resolution GCM. *Climate of the Past*, *8*(2), 723–740.

Botsyun, S., Mutz, S. G., Ehlers, T. A., Koptev, A., Wang, X., Schmidt, B., et al. (2022). Influence of large-scale atmospheric dynamics on precipitation seasonality of the Tibetan Plateau and Central Asia in cold and warm climates during the late cenozoic. *Journal of Geophysical Research: Atmospheres*, *127*(12), e2021JD035810. https://doi.org/10.1029/2021JD035810

Boyle, J., & Klein, S. A. (2010). Impact of horizontal resolution on climate model forecasts of tropical precipitation and diabatic heating for the TWP-ICE period. *Journal of Geophysical Research*, *115*(D23). https://doi.org/10.1029/2010JD014262

Braconnot, P., Harrison, S. P., Joussaume, S., Hewitt, C. D., Kitoch, A., Kutzbach, J. E., et al. (2004). Evaluation of PMIP coupled ocean-atmosphere simulations of the mid-Holocene. In R. W. Battarbee, F. Gasse, & C. E. Stickley (Eds.), *Past climate variability through Europe and Africa* (pp. 515–533). Springer Netherlands. https://doi.org/10.1007/978-1-4020-2121-3_24

Braconnot, P., Harrison, S. P., Kageyama, M., Bartlein, P. J., Masson-Delmotte, V., Abe-Ouchi, A., et al. (2012). Evaluation of climate models using palaeoclimatic data. *Nature Climate Change*, *2*(6), 417–424. https://doi.org/10.1038/nclimate1456

Braconnot, P., Otto-Bliesner, B., Harrison, S., Joussaume, S., Peterchmitt, J.-Y., Abe-Ouchi, A., et al. (2007). Results of PMIP2 coupled simulations of the Mid-Holocene and Last Glacial Maximum – Part 1: Experiments and large-scale features. *Climate of the Past*, *3*(2), 261–277. https://doi.org/10.5194/cp-3-261-2007

Brady, E. C., Otto-Bliesner, B. L., Kay, J. E., & Rosenbloom, N. (2013). Sensitivity to glacial forcing in the CCSM4. *Journal of Climate*, *26*(6), 1901–1925. https://doi.org/10.1175/JCLI-D-11-00416.1

Brierley, C. M., Zhao, A., Harrison, S. P., Braconnot, P., Williams, C. J. R., Thornalley, D. J. R., et al. (2020). Large-scale features and evaluation of the PMIP4-CMIP6 *midHolocene* simulations. *Climate of the Past*, *16*(5), 1847–1872. https://doi.org/10.5194/cp-16-1847-2020

Bühler, J. C., Axelsson, J., Lechleitner, F. A., Fohlmeister, J., LeGrande, A. N., Midhun, M., et al. (2022). Investigating stable oxygen and carbon isotopic variability in speleothem records over the last millennium using multiple isotope-enabled climate models. *Climate of the Past*, *18*(7), 1625–1654. https://doi.org/10.5194/cp-18-1625-2022

Burke, K. D., Williams, J. W., Chandler, M. A., Haywood, A. M., Lunt, D. J., & Otto-Bliesner, B. L. (2018). Pliocene and Eocene provide best analogs for near-future climates. *Proceedings of the National Academy of Sciences*, *115*(52), 13288–13293. https://doi.org/10.1073/pnas.1809600115

Cao, J., Wang, B., & Ma, L. (2019). Attribution of global monsoon response to the last glacial maximum forcings. *Journal of Climate*, *32*(19), 6589–6605. https://doi.org/10.1175/JCLI-D-18-0871.1

Cauquoin, A., Werner, M., & Lohmann, G. (2019). Water isotopes – Climate relationships for the mid-Holocene and preindustrial period simulated with an isotope-enabled version of MPI-ESM. *Climate of the Past*, *15*(6), 1913–1937. https://doi.org/10.5194/cp-15-1913-2019

Chandan, D., & Peltier, W. R. (2020). African Humid Period precipitation sustained by robust vegetation, soil, and lake feedbacks. *Geophysical Research Letters*, *47*(21), e2020GL088728. https://doi.org/10.1029/2020GL088728

Charney, J., Quirk, W. J., Chow, S., & Kornfield, J. (1977). A comparative study of the effects of albedo change on drought in semi-arid regions. *Journal of the Atmospheric Sciences*, *34*(9), 1366–1385. https://doi.org/10.1175/1520-0469(1977)034<1366:ACSOTE>2.0.CO;2

Cheng, H., Edwards, R. L., Sinha, A., Spötl, C., Yi, L., Chen, S., et al. (2016). The Asian monsoon over the past 640,000 years and ice age terminations. *Nature*, *534*(7609), 640–646. https://doi.org/10.1038/nature18591

Clark, P. U., Dyke, A. S., Shakun, J. D., Carlson, A. E., Clark, J., Wohlfarth, B., et al. (2009). The last glacial maximum. *Science*, *325*(5941), 710–714. https://doi.org/10.1126/science.1172873

Claussen, M., Kubatzki, C., Brovkin, V., Ganopolski, A., Hoelzmann, P., & Pachur, H.-J. (1999). Simulation of an abrupt change in Saharan vegetation in the Mid-Holocene. *Geophysical Research Letters*, *26*(14), 2037–2040. https://doi.org/10.1029/1999GL900494

CLIMAP, P. (1981). Seasonal reconstructions of the Earth's surface at the last glacial maximum. *Geological Society of America*.

Coe, M., & Harrison, S. (2002). The water balance of northern Africa during the mid-Holocene: An evaluation of the 6 ka BP PMIP simulations. *Climate Dynamics*, *19*(2), 155–166. https://doi.org/10.1007/s00382-001-0219-3

Cook, K. H. (2008). The mysteries of Sahel droughts. *Nature Geoscience*, *1*(10), 647–648. https://doi.org/10.1038/ngeo320

Corvec, S., & Fletcher, C. G. (2017). Changes to the tropical circulation in the mid-Pliocene and their implications for future climate. *Climate of the Past*, *13*(2), 135–147. https://doi.org/10.5194/cp-13-135-2017

Craig, H., & Gordon, L. I. (1965). Deuterium and oxygen 18 variations in the ocean and the marine atmosphere.
Cremaschi, M., & Di Lernia, S. (1999). Holocene climatic changes and cultural dynamics in the Libyan Sahara. *African Archaeological Review*, *16*(4), 211–238. https://doi.org/10.1023/A:1021609623737
Crook, J., Klein, C., Folwell, S., Taylor, C. M., Parker, D. J., Stratton, R., & Stein, T. (2019). Assessment of the representation of West African storm lifecycles in convection-permitting simulations. *Earth and Space Science*, *6*(5), 818–835. https://doi.org/10.1029/2018EA000491
D'Agostino, R., Bader, J., Bordoni, S., Ferreira, D., & Jungclaus, J. (2019). Northern hemisphere monsoon response to mid-Holocene orbital forcing and greenhouse gas-induced global warming. *Geophysical Research Letters*, *46*(3), 1591–1601. https://doi.org/10.1029/2018GL081589
D'Agostino, R., Brown, J. R., Moise, A., Nguyen, H., Dias, P. L. S., & Jungclaus, J. (2020). Contrasting Southern Hemisphere monsoon response: MidHolocene orbital forcing versus future greenhouse gas–induced global warming. *Journal of Climate*, *33*(22), 9595–9613. https://doi.org/10.1175/JCLI-D-19-0672.1
Dallmeyer, A., Claussen, M., Lorenz, S. J., & Shanahan, T. (2020). The end of the African humid period as seen by a transient comprehensive Earth system model simulation of the last 8000 years. *Climate of the Past*, *16*(1), 117–140. https://doi.org/10.5194/cp-16-117-2020
Dansgaard, W., Johnsen, S. J., Clausen, H. B., Dahl-Jensen, D., Gundestrup, N. S., Hammer, C. U., et al. (1993). Evidence for general instability of past climate from a 250-kyr ice-core record. *Nature*, *364*(6434), 218–220. https://doi.org/10.1038/364218a0
de la Vega, E., Chalk, T. B., Wilson, P. A., Bysani, R. P., & Foster, G. L. (2020). Atmospheric CO_2 during the mid-Piacenzian warm period and the M2 glaciation. *Scientific Reports*, *10*(1), 11002. https://doi.org/10.1038/s41598-020-67154-8
deMenocal, P., Ortiz, J., Guilderson, T., Adkins, J., Sarnthein, M., Baker, L., & Yarusinsky, M. (2000). Abrupt onset and termination of the African Humid Period: Rapid climate responses to gradual insolation forcing. *Quaternary Science Reviews*, *19*(1), 347–361. https://doi.org/10.1016/S0277-3791(99)00081-5
deMenocal, P. B. (2004). African climate change and faunal evolution during the Pliocene–Pleistocene. *Earth and Planetary Science Letters*, *220*(1), 3–24. https://doi.org/10.1016/S0012-821X(04)00003-2
de Nooijer, W., Zhang, Q., Li, Q., Zhang, Q., Li, X., Zhang, Z., et al. (2020). Evaluation of Arctic warming in mid-Pliocene climate simulations. *Climate of the Past*, *16*(6), 2325–2341. https://doi.org/10.5194/cp-16-2325-2020
Dietrich, S., Werner, M., Spangehl, T., & Lohmann, G. (2013). Influence of orbital forcing and solar activity on water isotopes in precipitation during the mid- and late Holocene. *Climate of the Past*, *9*(1), 13–26. https://doi.org/10.5194/cp-9-13-2013
Dowsett, H., Dolan, A., Rowley, D., Moucha, R., Forte, A. M., Mitrovica, J. X., et al. (2016). The PRISM4 (mid-Piacenzian) paleoenvironmental reconstruction. *Climate of the Past*, *12*(7), 1519–1538. https://doi.org/10.5194/cp-12-1519-2016
Dowsett, H., Robinson, M., Haywood, A. M., Salzmann, U., Hill, D., Sohl, L. E., et al. (2010). The PRISM3D paleoenvironmental reconstruction. *Stratigraphy*.
Dunne, J., Evershed, R. P., Salque, M., Cramp, L., Bruni, S., Ryan, K., et al. (2012). First dairying in green Saharan Africa in the fifth millennium BC. *Nature*, *486*(7403), 390–394. https://doi.org/10.1038/nature11186
Egerer, S., Claussen, M., & Reick, C. (2018). Rapid increase in simulated North Atlantic dust deposition due to fast change of northwest African landscape during the Holocene. *Climate of the Past*, *14*(7), 1051–1066. https://doi.org/10.5194/cp-14-1051-2018
Elenga, H., Peyron, O., Bonnefille, R., Jolly, D., Cheddadi, R., Guiot, J., et al. (2000). Pollen-based biome reconstruction for southern Europe and Africa 18,000 yr bp. *Journal of Biogeography*, *27*(3), 621–634. https://doi.org/10.1046/j.1365-2699.2000.00430.x
Erfanian, A., Wang, G., Yu, M., & Anyah, R. (2016). Multimodel ensemble simulations of present and future climates over West Africa: Impacts of vegetation dynamics. *Journal of Advances in Modeling Earth Systems*, *8*(3), 1411–1431. https://doi.org/10.1002/2016MS000660
Etheridge, D. M., Steele, L. P., Francey, R. J., & Langenfelds, R. L. (1998). Atmospheric methane between 1000 A.D. and present: Evidence of anthropogenic emissions and climatic variability. *Journal of Geophysical Research*, *103*(D13), 15979–15993. https://doi.org/10.1029/98JD00923
Etheridge, D. M., Steele, L. P., Langenfelds, R. L., Francey, R. J., Barnola, J.-M., & Morgan, V. I. (1996). Natural and anthropogenic changes in atmospheric CO_2 over the last 1000 years from air in Antarctic ice and firn. *Journal of Geophysical Research*, *101*(D2), 4115–4128. https://doi.org/10.1029/95JD03410
Evan, A. T., Flamant, C., Fiedler, S., & Doherty, O. (2014). An analysis of aeolian dust in climate models. *Geophysical Research Letters*, *41*(16), 5996–6001. https://doi.org/10.1002/2014GL060545
Eyring, V., Bony, S., Meehl, G. A., Senior, C. A., Stevens, B., Stouffer, R. J., & Taylor, K. E. (2016). Overview of the coupled model Intercomparison project phase 6 (CMIP6) experimental design and organization. *Geoscientific Model Development*, *9*(5), 1937–1958. https://doi.org/10.5194/gmd-9-1937-2016
Feng, R., Bhattacharya, T., Otto-Bliesner, B. L., Brady, E. C., Haywood, A. M., Tindall, J. C., et al. (2022). Past terrestrial hydroclimate sensitivity controlled by Earth system feedbacks. *Nature Communications*, *13*(1), 1306. https://doi.org/10.1038/s41467-022-28814-7
Friedrich, T., Timmermann, A., Tigchelaar, M., Elison Timm, O., & Ganopolski, A. (2016). Nonlinear climate sensitivity and its implications for future greenhouse warming. *Science Advances*, *2*(11), e1501923. https://doi.org/10.1126/sciadv.1501923
Gabriel, B. (1987). Palaeoecological evidence from neolithic fireplaces in the Sahara. *African Archaeological Review*, *5*(1), 93–103. https://doi.org/10.1007/BF01117085
Gaetani, M., Messori, G., Zhang, Q., Flamant, C., & Pausata, F. S. R. (2017). Understanding the mechanisms behind the northward extension of the West African monsoon during the mid-Holocene. *Journal of Climate*, *30*(19), 7621–7642. https://doi.org/10.1175/JCLI-D-16-0299.1
Gao, X., Xu, Y., Zhao, Z., Pal, J. S., & Giorgi, F. (2006). On the role of resolution and topography in the simulation of East Asia precipitation. *Theoretical and Applied Climatology*, *86*(1), 173–185. https://doi.org/10.1007/s00704-005-0214-4
Gill, A. E. (1980). Some simple solutions for heat-induced tropical circulation. *Quarterly Journal of the Royal Meteorological Society*, *106*(449), 447–462. https://doi.org/10.1002/qj.49710644905
Grist, J. P. (2002). Easterly waves over Africa. Part I: The seasonal cycle and contrasts between wet and dry years. *Monthly Weather Review*, *130*(2), 197–211. https://doi.org/10.1175/1520-0493(2002)130<0197:EWOAPI>2.0.CO;2
Hagemann, S. (2002). Validierung des Niederschlags in globalen Klimamodellen. 5. Workshop Zur Hydrologischen Modellierung: Möglichkeiten Und Grenzen Für Den Einsatz Hydrologischer Modelle in Politik, Wirtschaft Und Klimafolgenforschung (pp. 115–127).
Hagemann, S., Arpe, K., & Roeckner, E. (2006). Evaluation of the hydrological cycle in the ECHAM5 model. *Journal of Climate*, *19*(16), 3810–3827. https://doi.org/10.1175/JCLI3831.1
Harris, I., Jones, P. d., Osborn, T. j., & Lister, D. h. (2014). Updated high-resolution grids of monthly climatic observations – The CRU TS3.10 dataset. *International Journal of Climatology*, *34*(3), 623–642. https://doi.org/10.1002/joc.3711
Harris, I., Osborn, T. J., Jones, P., & Lister, D. (2020). Version 4 of the CRU TS monthly high-resolution gridded multivariate climate dataset. *Scientific Data*, *7*(1), 109. https://doi.org/10.1038/s41597-020-0453-3

Harrison, S. P., Bartlein, P. J., Brewer, S., Prentice, I. C., Boyd, M., Hessler, I., et al. (2014). Climate model benchmarking with glacial and mid-Holocene climates. *Climate Dynamics*, *43*(3), 671–688. https://doi.org/10.1007/s00382-013-1922-6

Harrison, S. P., Bartlein, P. J., Izumi, K., Li, G., Annan, J., Hargreaves, J., et al. (2015). Evaluation of CMIP5 palaeo-simulations to improve climate projections. *Nature Climate Change*, *5*(8), 735–743. https://doi.org/10.1038/nclimate2649

Harrison, S. P., Yu, G., Takahara, H., & Prentice, I. C. (2001). Diversity of temperate plants in east Asia. *Nature*, *413*(6852), 129–130. https://doi.org/10.1038/35093166

Haywood, A. M., Dowsett, H. J., Dolan, A. M., Rowley, D., Abe-Ouchi, A., Otto-Bliesner, B., et al. (2016). The Pliocene model Intercomparison project (PlioMIP) phase 2: Scientific objectives and experimental design. *Climate of the Past*, *12*(3), 663–675. https://doi.org/10.5194/cp-12-663-2016

Haywood, A. M., Dowsett, H. J., Otto-Bliesner, B., Chandler, M. A., Dolan, A. M., Hill, D. J., et al. (2010). Pliocene model Intercomparison project (PlioMIP): Experimental design and boundary conditions (experiment 1). *Geoscientific Model Development*, *3*(1), 227–242. https://doi.org/10.5194/gmd-3-227-2010

Haywood, A. M., Hill, D. J., Dolan, A. M., Otto-Bliesner, B. L., Bragg, F., Chan, W.-L., et al. (2013). Large-scale features of Pliocene climate: Results from the Pliocene model Intercomparison project. *Climate of the Past*, *9*(1), 191–209. https://doi.org/10.5194/cp-9-191-2013

Haywood, A. M., Tindall, J. C., Dowsett, H. J., Dolan, A. M., Foley, K. M., Hunter, S. J., et al. (2020). The Pliocene model Intercomparison project phase 2: Large-scale climate features and climate sensitivity. *Climate of the Past*, *16*(6), 2095–2123. https://doi.org/10.5194/cp-16-2095-2020

Hersbach, H., Bell, B., Berrisford, P., Hirahara, S., Horányi, A., Muñoz-Sabater, J., et al. (2020). The ERA5 global reanalysis. *Quarterly Journal of the Royal Meteorological Society*, *146*(730), 1999–2049. https://doi.org/10.1002/qj.3803

Hoelzmann, P., Jolly, D., Harrison, S. P., Laarif, F., Bonnefille, R., & Pachur, H.-J. (1998). Mid-Holocene land-surface conditions in northern Africa and the Arabian peninsula: A data set for the analysis of biogeophysical feedbacks in the climate system. *Global Biogeochemical Cycles*, *12*(1), 35–51. https://doi.org/10.1029/97GB02733

Hoelzmann, P., Keding, B., Berke, H., Kröpelin, S., & Kruse, H.-J. (2001). Environmental change and archaeology: Lake evolution and human occupation in the eastern Sahara during the holocene. *Palaeogeography, Palaeoclimatology, Palaeoecology*, *169*(3), 193–217. https://doi.org/10.1016/S0031-0182(01)00211-5

Holmes, J. A. (2008). How the Sahara became dry. *Science*, *320*(5877), 752–753. https://doi.org/10.1126/science.1158105

Hopcroft, P. O., & Valdes, P. J. (2019). On the role of dust-climate feedbacks during the mid-Holocene. *Geophysical Research Letters*, *46*(3), 1612–1621. https://doi.org/10.1029/2018GL080483

Hopcroft, P. O., & Valdes, P. J. (2022). Green Sahara tipping points in transient climate model simulations of the Holocene. *Environmental Research Letters*, *17*(8), 085001. https://doi.org/10.1088/1748-9326/ac7c2b

Janicot, S., Caniaux, G., Chauvin, F., de Coëtlogon, G., Fontaine, B., Hall, N., et al. (2011). Intraseasonal variability of the West African monsoon. *Atmospheric Science Letters*, *12*(1), 58–66. https://doi.org/10.1002/asl.280

Jenkins, G. S., Gaye, A. T., & Sylla, B. (2005). Late 20th century attribution of drying trends in the Sahel from the regional Climate model (RegCM3). *Geophysical Research Letters*, *32*(22). https://doi.org/10.1029/2005GL024225

Jiang, D., Tian, Z., Lang, X., Kageyama, M., & Ramstein, G. (2015). The concept of global monsoon applied to the last glacial maximum: A multi-model analysis. *Quaternary Science Reviews*, *126*, 126–139. https://doi.org/10.1016/j.quascirev.2015.08.033

Jiang, D., Wang, H., Ding, Z., Lang, X., & Drange, H. (2005). Modeling the middle Pliocene climate with a global atmospheric general circulation model. *Journal of Geophysical Research*, *110*(D14). https://doi.org/10.1029/2004JD005639

Jolly, D., Prentice, I. C., Bonnefille, R., Ballouche, A., Bengo, M., Brenac, P., et al. (1998). Biome reconstruction from pollen and plant macrofossil data for Africa and the Arabian peninsula at 0 and 6000 years. *Journal of Biogeography*, *25*(6), 1007–1027. https://doi.org/10.1046/j.1365-2699.1998.00238.x

Joussaume, S., Taylor, K. E., Braconnot, P., Mitchell, J. F. B., Kutzbach, J. E., Harrison, S. P., et al. (1999). Monsoon changes for 6000 years ago: Results of 18 simulations from the paleoclimate modeling Intercomparison project (PMIP). *Geophysical Research Letters*, *26*(7), 859–862. https://doi.org/10.1029/1999GL900126

Jungandreas, L., Hohenegger, C., & Claussen, M. (2021). Influence of the representation of convection on the mid-Holocene West African monsoon. *Climate of the Past*, *17*(4), 1665–1684. https://doi.org/10.5194/cp-17-1665-2021

Kageyama, M., Braconnot, P., Bopp, L., Caubel, A., Foujols, M.-A., Guilyardi, E., et al. (2013). Mid-Holocene and Last Glacial Maximum climate simulations with the IPSL model—Part I: Comparing IPSL_CM5A to IPSL_CM4. *Climate Dynamics*, *40*(9), 2447–2468. https://doi.org/10.1007/s00382-012-1488-8

Kageyama, M., Braconnot, P., Harrison, S. P., Haywood, A. M., Jungclaus, J. H., Otto-Bliesner, B. L., et al. (2018). The PMIP4 contribution to CMIP6 – Part 1: Overview and over-arching analysis plan. *Geoscientific Model Development*, *11*(3), 1033–1057. https://doi.org/10.5194/gmd-11-1033-2018

Kageyama, M., Harrison, S. P., Kapsch, M.-L., Lofverstrom, M., Lora, J. M., Mikolajewicz, U., et al. (2021). The PMIP4 Last Glacial Maximum experiments: Preliminary results and comparison with the PMIP3 simulations. *Climate of the Past*, *17*(3), 1065–1089. https://doi.org/10.5194/cp-17-1065-2021

Kim, S.-J., Crowley, T. J., Erickson, D. J., Govindasamy, B., Duffy, P. B., & Lee, B. Y. (2008). High-resolution climate simulation of the last glacial maximum. *Climate Dynamics*, *31*(1), 1–16. https://doi.org/10.1007/s00382-007-0332-z

Klein, C., Bliefernicht, J., Heinzeller, D., Gessner, U., Klein, I., & Kunstmann, H. (2017). Feedback of observed interannual vegetation change: A regional climate model analysis for the West African monsoon. *Climate Dynamics*, *48*(9), 2837–2858. https://doi.org/10.1007/s00382-016-3237-x

Kohfeld, K. E., & Harrison, S. P. (2000). How well can we simulate past climates? Evaluating the models using global palaeoenvironmental datasets. *Quaternary Science Reviews*, *19*(1), 321–346. https://doi.org/10.1016/S0277-3791(99)00068-2

Kok, J. F. (2010). An improved parameterization of wind-blown sand flux on Mars that includes the effect of hysteresis. *Geophysical Research Letters*, *37*(12). https://doi.org/10.1029/2010GL043646

Kolstad, E. W., & Screen, J. A. (2019). Nonstationary relationship between autumn Arctic sea ice and the winter North Atlantic oscillation. *Geophysical Research Letters*, *46*(13), 7583–7591. https://doi.org/10.1029/2019GL083059

Kröpelin, S., Verschuren, D., Lézine, A.-M., Eggermont, H., Cocquyt, C., Francus, P., et al. (2008). Climate-driven ecosystem succession in the Sahara: The past 6000 years. *Science*, *320*(5877), 765–768. https://doi.org/10.1126/science.1154913

Kuechler, R. R., Dupont, L. M., & Schefuß, E. (2018). Hybrid insolation forcing of Pliocene monsoon dynamics in West Africa. *Climate of the Past*, *14*(1), 73–84. https://doi.org/10.5194/cp-14-73-2018

Kutzbach, J. E., & Liu, Z. (1997). Response of the African monsoon to orbital forcing and ocean feedbacks in the middle Holocene. *Science*, *278*(5337), 440–443. https://doi.org/10.1126/science.278.5337.440

Lambeck, K., Rouby, H., Purcell, A., Sun, Y., & Sambridge, M. (2014). Sea level and global ice volumes from the Last Glacial Maximum to the Holocene. *Proceedings of the National Academy of Sciences*, *111*(43), 15296–15303. https://doi.org/10.1073/pnas.1411762111

Lavaysse, C., Flamant, C., Janicot, S., Parker, D. J., Lafore, J.-P., Sultan, B., & Pelon, J. (2009). Seasonal evolution of the West African heat low: A climatological perspective. *Climate Dynamics*, *33*(2), 313–330. https://doi.org/10.1007/s00382-009-0553-4

Lawrence, J. R., Gedzelman, S. D., Dexheimer, D., Cho, H.-K., Carrie, G. D., Gasparini, R., et al. (2004). Stable isotopic composition of water vapor in the tropics. *Journal of Geophysical Research*, *109*(D6). https://doi.org/10.1029/2003JD004046

LeGrande, A. N., & Schmidt, G. A. (2006). Global gridded data set of the oxygen isotopic composition in seawater. *Geophysical Research Letters*, *33*(12). https://doi.org/10.1029/2006GL026011

Lemburg, A., Bader, J., & Claussen, M. (2019). Sahel rainfall–tropical easterly jet relationship on synoptic to intraseasonal time scales. *Monthly Weather Review*, *147*(5), 1733–1752. https://doi.org/10.1175/MWR-D-18-0254.1

Leung, D. M., Kok, J. F., Li, L., Okin, G. S., Prigent, C., Klose, M., et al. (2023). A new process-based and scale-aware desert dust emission scheme for global climate models – Part I: Description and evaluation against inverse modeling emissions. *Atmospheric Chemistry and Physics*, *23*(11), 6487–6523. https://doi.org/10.5194/acp-23-6487-2023

Levis, S., Bonan, G. B., & Bonfils, C. (2004). Soil feedback drives the mid-Holocene North African monsoon northward in fully coupled CCSM2 simulations with a dynamic vegetation model. *Climate Dynamics*, *23*(7), 791–802. https://doi.org/10.1007/s00382-004-0477-y

Li, X., Jiang, D., Tian, Z., & Yang, Y. (2018). Mid-Pliocene global land monsoon from PlioMIP1 simulations. *Palaeogeography, Palaeoclimatology, Palaeoecology*, *512*, 56–70. https://doi.org/10.1016/j.palaeo.2018.06.027

Li, X., Jiang, D., Zhang, Z., Zhang, R., Tian, Z., & Yan, Q. (2015). Mid-Pliocene westerlies from PlioMIP simulations. *Advances in Atmospheric Sciences*, *32*(7), 909–923. https://doi.org/10.1007/s00376-014-4171-7

Liakka, J., & Lofverstrom, M. (2018). Arctic warming induced by the Laurentide ice sheet topography. *Climate of the Past*, *14*(6), 887–900. https://doi.org/10.5194/cp-14-887-2018

Liakka, J., Löfverström, M., & Colleoni, F. (2016). The impact of the North American glacial topography on the evolution of the Eurasian ice sheet over the last glacial cycle. *Climate of the Past*, *12*(5), 1225–1241. https://doi.org/10.5194/cp-12-1225-2016

Lohmann, G., Pfeiffer, M., Laepple, T., Leduc, G., & Kim, J.-H. (2013). A model–data comparison of the Holocene global sea surface temperature evolution. *Climate of the Past*, *9*(4), 1807–1839. https://doi.org/10.5194/cp-9-1807-2013

Lohmann, U., & Roeckner, E. (1996). Design and performance of a new cloud microphysics scheme developed for the ECHAM general circulation model. *Climate Dynamics*, *12*(8), 557–572. https://doi.org/10.1007/BF00207939

Lora, J. M. (2018). Components and mechanisms of hydrologic cycle changes over North America at the last glacial maximum. *Journal of Climate*, *31*(17), 7035–7051. https://doi.org/10.1175/JCLI-D-17-0544.1

Lorenz, S. J., & Lohmann, G. (2004). Acceleration technique for Milankovitch type forcing in a coupled atmosphere-ocean circulation model: Method and application for the Holocene. *Climate Dynamics*, *23*(7–8), 727–743. https://doi.org/10.1007/s00382-004-0469-y

Manning, K., & Timpson, A. (2014). The demographic response to Holocene climate change in the Sahara. *Quaternary Science Reviews*, *101*, 28–35. https://doi.org/10.1016/j.quascirev.2014.07.003

Marsham, J. H., Dixon, N. S., Garcia-Carreras, L., Lister, G. M. S., Parker, D. J., Knippertz, P., & Birch, C. E. (2013). The role of moist convection in the West African monsoon system: Insights from continental-scale convection-permitting simulations. *Geophysical Research Letters*, *40*(9), 1843–1849. https://doi.org/10.1002/grl.50347

Marzin, C., & Braconnot, P. (2009). Variations of Indian and African monsoons induced by insolation changes at 6 and 9.5 kyr BP. *Climate Dynamics*, *33*(2), 215–231. https://doi.org/10.1007/s00382-009-0538-3

McManus, J. F., Francois, R., Gherardi, J.-M., Keigwin, L. D., & Brown-Leger, S. (2004). Collapse and rapid resumption of Atlantic meridional circulation linked to deglacial climate changes. *Nature*, *428*(6985), 834–837. https://doi.org/10.1038/nature02494

Messori, G., Gaetani, M., Zhang, Q., Zhang, Q., & Pausata, F. S. R. (2019). The water cycle of the mid-Holocene West African monsoon: The role of vegetation and dust emission changes. *International Journal of Climatology*, *39*(4), 1927–1939. https://doi.org/10.1002/joc.5924

Mulitza, S., Prange, M., Stuut, J.-B., Zabel, M., von Dobeneck, T., Itambi, A. C., et al. (2008). Sahel megadroughts triggered by glacial slowdowns of Atlantic meridional overturning. *Paleoceanography*, *23*(4). https://doi.org/10.1029/2008PA001637

Mutz, S. G., Ehlers, T. A., Werner, M., Lohmann, G., Stepanek, C., & Li, J. (2018). Estimates of late Cenozoic climate change relevant to Earth surface processes in tectonically active orogens. *Earth Surface Dynamics*, *6*(2), 271–301. https://doi.org/10.5194/esurf-6-271-2018

Newell, R. E., & Kidson, J. W. (1984). African mean wind changes between sahelian wet and dry periods. *Journal of Climatology*, *4*(1), 27–33. https://doi.org/10.1002/joc.3370040103

Nicholson, S. E. (2008). The intensity, location and structure of the tropical rainbelt over west Africa as factors in interannual variability. *International Journal of Climatology*, *28*(13), 1775–1785. https://doi.org/10.1002/joc.1507

Nicholson, S. E. (2009). On the factors modulating the intensity of the tropical rainbelt over West Africa. *International Journal of Climatology*, *29*(5), 673–689.%2010.1002/joc.1702

Nicholson, S. E., & Klotter, D. (2021). The Tropical Easterly Jet over Africa, its representation in six reanalysis products, and its association with Sahel rainfall. *International Journal of Climatology*, *41*(1), 328–347. https://doi.org/10.1002/joc.6623

Nicholson, S. E., & Grist, J. p. (2001). A conceptual model for understanding rainfall variability in the West African Sahel on interannual and interdecadal timescales. *International Journal of Climatology*, *21*(14), 1733–1757. https://doi.org/10.1002/joc.648

Nicholson, S. E., & Grist, J. P. (2003). The seasonal evolution of the atmospheric circulation over West Africa and equatorial Africa. *Journal of Climate*, *16*(7), 1013–1030. https://doi.org/10.1175/1520-0442(2003)016<1013:TSEOTA>2.0.CO;2

Nicholson, S. E., & Palao, I. M. (1993). A re-evaluation of rainfall variability in the sahel. Part I. Characteristics of rainfall fluctuations. *International Journal of Climatology*, *13*(4), 371–389. https://doi.org/10.1002/joc.3370130403

Nicholson, S. E., & Webster, P. J. (2007). A physical basis for the interannual variability of rainfall in the Sahel. *Quarterly Journal of the Royal Meteorological Society*, *133*(629), 2065–2084. https://doi.org/10.1002/qj.104

Notaro, M., Wang, Y., Liu, Z., Gallimore, R., & Levis, S. (2008). Combined statistical and dynamical assessment of simulated vegetation–rainfall interactions in North Africa during the mid-Holocene1. *Global Change Biology*, *14*(2), 347–368. https://doi.org/10.1111/j.1365-2486.2007.01495.x

Otto-Bliesner, B. L., Braconnot, P., Harrison, S. P., Lunt, D. J., Abe-Ouchi, A., Albani, S., et al. (2017). The PMIP4 contribution to CMIP6 – Part 2: Two interglacials, scientific objective and experimental design for Holocene and Last Interglacial simulations. *Geoscientific Model Development*, *10*(11), 3979–4003. https://doi.org/10.5194/gmd-10-3979-2017

Otto-Bliesner, B. L., Brady, E. C., Clauzet, G., Tomas, R., Levis, S., & Kothavala, Z. (2006). Last Glacial Maximum and Holocene climate in CCSM3. *Journal of Climate*, *19*(11), 2526–2544. https://doi.org/10.1175/JCLI3748.1

Patricola, C. M., & Cook, K. H. (2007). Dynamics of the West African monsoon under Mid-Holocene precessional forcing: Regional climate model simulations. *Journal of Climate*, *20*(4), 694–716. https://doi.org/10.1175/JCLI4013.1

Pausata, F. S. R., Gaetani, M., Messori, G., Berg, A., Maia de Souza, D., Sage, R. F., & deMenocal, P. B. (2020). The greening of the Sahara: Past changes and future implications. *One Earth*, *2*(3), 235–250. https://doi.org/10.1016/j.oneear.2020.03.002

Pausata, F. S. R., Messori, G., & Zhang, Q. (2016). Impacts of dust reduction on the northward expansion of the African monsoon during the Green Sahara period. *Earth and Planetary Science Letters*, *434*, 298–307. https://doi.org/10.1016/j.epsl.2015.11.049

Peltier, W. R., & Fairbanks, R. G. (2006). Global glacial ice volume and Last Glacial Maximum duration from an extended Barbados sea level record. *Quaternary Science Reviews*, *25*(23), 3322–3337. https://doi.org/10.1016/j.quascirev.2006.04.010

Perez-Sanz, A., Li, G., González-Sampériz, P., & Harrison, S. P. (2014). Evaluation of modern and mid-Holocene seasonal precipitation of the Mediterranean and northern Africa in the CMIP5 simulations. *Climate of the Past*, *10*(2), 551–568. https://doi.org/10.5194/cp-10-551-2014

Peyron, O., Jolly, D., Braconnot, P., Bonnefille, R., Guiot, J., Wirrmann, D., & Chalié, F. (2006). Quantitative reconstructions of annual rainfall in Africa 6000 years ago: Model-data comparison. *Journal of Geophysical Research*, *111*(D24). https://doi.org/10.1029/2006JD007396

Phipps, S. J., McGregor, H. V., Gergis, J., Gallant, A. J. E., Neukom, R., Stevenson, S., et al. (2013). Paleoclimate data–model comparison and the role of climate forcings over the past 1500 years. *Journal of Climate*, *26*(18), 6915–6936. https://doi.org/10.1175/JCLI-D-12-00108.1

Pickett, E. J., Harrison, S. P., Hope, G., Harle, K., Dodson, J. R., Peter Kershaw, A., et al. (2004). Pollen-based reconstructions of biome distributions for Australia, Southeast Asia and the Pacific (SEAPAC region) at 0, 6000 and 18,000 14C yr BP. *Journal of Biogeography*, *31*(9), 1381–1444. https://doi.org/10.1111/j.1365-2699.2004.01001.x

Prentice, I. C., Jolly, D., & Participants, B. (2000). Mid-Holocene and glacial-maximum vegetation geography of the northern continents and Africa. *Journal of Biogeography*, *27*(3), 507–519. https://doi.org/10.1046/j.1365-2699.2000.00425.x

Quagraine, K. A., Nkrumah, F., Klein, C., Klutse, N. A. B., & Quagraine, K. T. (2020). West African summer monsoon precipitation variability as represented by reanalysis datasets. *Climate*, *8*(10), 111. https://doi.org/10.3390/cli8100111

Rachmayani, R., Prange, M., & Schulz, M. (2015). North African vegetation–precipitation feedback in early and mid-Holocene climate simulations with CCSM3-DGVM. *Climate of the Past*, *11*(2), 175–185. https://doi.org/10.5194/cp-11-175-2015

Raible, C. C., Lehner, F., González-Rouco, J. F., & Fernández-Donado, L. (2014). Changing correlation structures of the Northern Hemisphere atmospheric circulation from 1000 to 2100 AD. *Climate of the Past*, *10*(2), 537–550. https://doi.org/10.5194/cp-10-537-2014

Redelsperger, J.-L., Parsons, D. B., & Guichard, F. (2002). Recovery processes and factors limiting cloud-top height following the arrival of a dry intrusion observed during TOGA COARE. *Journal of the Atmospheric Sciences*, *59*(16), 2438–2457. https://doi.org/10.1175/1520-0469(2002)059<2438:RPAFLC>2.0.CO;2

Risi, C., Bony, S., Vimeux, F., Descroix, L., Ibrahim, B., Lebreton, E., et al. (2008). What controls the isotopic composition of the African monsoon precipitation? Insights from event-based precipitation collected during the 2006 AMMA field campaign. *Geophysical Research Letters*, *35*(24). https://doi.org/10.1029/2008GL035920

Risi, C., Bony, S., Vimeux, F., Frankenberg, C., Noone, D., & Worden, J. (2010). Understanding the Sahelian water budget through the isotopic composition of water vapor and precipitation. *Journal of Geophysical Research*, *115*(D24). https://doi.org/10.1029/2010JD014690

Risi, C., Noone, D., Frankenberg, C., & Worden, J. (2013). Role of continental recycling in intraseasonal variations of continental moisture as deduced from model simulations and water vapor isotopic measurements: Continental Recycling and Water Isotopes. *Water Resources Research*, *49*(7), 4136–4156. https://doi.org/10.1002/wrcr.20312

Risi, C., Noone, D., Worden, J., Frankenberg, C., Stiller, G., Kiefer, M., et al. (2012). Process-evaluation of tropospheric humidity simulated by general circulation models using water vapor isotopologues: 1. Comparison between models and observations. *Journal of Geophysical Research*, *117*(D5). https://doi.org/10.1029/2011JD016621

Roeckner, E., Bäuml, G., Bonaventura, L., Brokopf, R., Esch, M., Giorgetta, M., et al. (2003). The atmospheric general circulation model ECHAM 5. PART I. *Model description*. https://doi.org/10.17617/2.995269

Roehrig, R., Bouniol, D., Guichard, F., Hourdin, F., & Redelsperger, J.-L. (2013). The present and future of the West African monsoon: A process-oriented assessment of CMIP5 simulations along the AMMA transect. *Journal of Climate*, *26*(17), 6471–6505. https://doi.org/10.1175/JCLI-D-12-00505.1

Rozanski, K., Araguás-Araguás, L., & Gonfiantini, R. (1993). Climate change in continental isotopic records. Retrieved from https://scholar.google.com/scholar_lookup?hl=en&publication_year=1993&pages=1-36&author=K.+Rozanski&author=L.+Aragu%C3%A1s%E2%80%90Aragu%C3%A1s&author=R.+Gonfiantini&title=Climate+Change+in+Continental+Isotopic+Records

Salzmann, U., Dolan, A. M., Haywood, A. M., Chan, W.-L., Voss, J., Hill, D. J., et al. (2013). Challenges in quantifying Pliocene terrestrial warming revealed by data–model discord. *Nature Climate Change*, *3*(11), 969–974. https://doi.org/10.1038/nclimate2008

Salzmann, U., Haywood, A. M., Lunt, D. J., Valdes, P. J., & Hill, D. J. (2008). A new global biome reconstruction and data-model comparison for the Middle Pliocene. *Global Ecology and Biogeography*, *17*(3), 432–447. https://doi.org/10.1111/j.1466-8238.2008.00381.x

Samakinwa, E., Stepanek, C., & Lohmann, G. (2020). Sensitivity of mid-Pliocene climate to changes in orbital forcing and PlioMIP's boundary conditions. *Climate of the Past*, *16*(4), 1643–1665. https://doi.org/10.5194/cp-16-1643-2020

Sarnthein, M., Gersonde, R., Niebler, S., Pflaumann, U., Spielhagen, R., Thiede, J., et al. (2003). Overview of glacial Atlantic Ocean mapping (GLAMAP 2000). *Paleoceanography*, *18*(2). https://doi.org/10.1029/2002PA000769

Scheff, J., & Frierson, D. M. W. (2012). Robust future precipitation declines in CMIP5 largely reflect the poleward expansion of model subtropical dry zones. *Geophysical Research Letters*, *39*(18). https://doi.org/10.1029/2012GL052910

Seager, R., & Henderson, N. (2013). Diagnostic computation of moisture budgets in the ERA-interim reanalysis with reference to analysis of CMIP-archived atmospheric model data. *Journal of Climate*, *26*(20), 7876–7901. https://doi.org/10.1175/JCLI-D-13-00018.1

Sereno, P. C., Garcea, E. A. A., Jousse, H., Stojanowski, C. M., Saliège, J.-F., Maga, A., et al. (2008). Lakeside cemeteries in the Sahara: 5000 Years of Holocene population and environmental change. *PLoS One*, *3*(8), e2995. https://doi.org/10.1371/journal.pone.0002995

Seth, A., Giannini, A., Rojas, M., Rauscher, S. A., Bordoni, S., Singh, D., & Camargo, S. J. (2019). Monsoon responses to climate changes—Connecting past, present and future. *Current Climate Change Reports*, *5*(2), 63–79. https://doi.org/10.1007/s40641-019-00125-y

Sha, L., Ait Brahim, Y., Wassenburg, J. A., Yin, J., Peros, M., Cruz, F. W., et al. (2019). How far north did the African monsoon fringe expand during the African Humid Period? Insights from southwest Moroccan speleothems. *Geophysical Research Letters*, *46*(23), 14093–14102. https://doi.org/10.1029/2019GL084879

Shi, X., Cauquoin, A., Lohmann, G., Jonkers, L., Wang, Q., Yang, H., et al. (2023). Simulated stable water isotopes during the mid-Holocene and pre-industrial using AWI-ESM-2.1-wiso. *Geoscientific Model Development Discussions*, 1–39. https://doi.org/10.5194/gmd-2023-68

Shi, X., Lohmann, G., Sidorenko, D., & Yang, H. (2020). Early-Holocene simulations using different forcings and resolutions in AWI-ESM. *The Holocene*, *30*(7), 996–1015. https://doi.org/10.1177/0959683620908634

Simmons, A. J., Burridge, D. M., Jarraud, M., Girard, C., & Wergen, W. (1989). The ECMWF medium-range prediction models development of the numerical formulations and the impact of increased resolution. *Meteorology and Atmospheric Physics*, *40*(1), 28–60. https://doi.org/10.1007/BF01027467

Sohl, L. E., Chandler, M. A., Schmunk, R. B., Mankoff, K., Jonas, J. A., Foley, K. M., & Dowsett, H. J. (2009). *PRISM3/GISS topographic reconstruction (No. 419). Data series*. U.S. Geological Survey. https://doi.org/10.3133/ds419

Sperber, K. R., Hameed, S., Potter, G. L., & Boyle, J. S. (1994). Simulation of the northern summer monsoon in the ECMWF model: Sensitivity to horizontal resolution. *Monthly Weather Review*, *122*(11), 2461–2481. https://doi.org/10.1175/1520-0493(1994)122<2461:SOTNSM>2.0.CO;2

Stager, J. C., Mayewski, P. A., & Meeker, L. D. (2002). Cooling cycles, Heinrich event 1, and the desiccation of Lake Victoria. *Palaeogeography, Palaeoclimatology, Palaeoecology*, *183*(1), 169–178. https://doi.org/10.1016/S0031-0182(01)00468-0

Stager, J. C., Ryves, D. B., Chase, B. M., & Pausata, F. S. R. (2011). Catastrophic drought in the Afro-Asian monsoon region during Heinrich event 1. *Science*, *331*(6022), 1299–1302. https://doi.org/10.1126/science.1198322

Stepanek, C., & Lohmann, G. (2012). Modelling mid-Pliocene climate with COSMOS. *Geoscientific Model Development*, *5*(5), 1221–1243. https://doi.org/10.5194/gmd-5-1221-2012

Stepanek, C., Samakinwa, E., Knorr, G., & Lohmann, G. (2020). Contribution of the coupled atmosphere–ocean–sea ice–vegetation model COSMOS to the PlioMIP2. *Climate of the Past*, *16*(6), 2275–2323. https://doi.org/10.5194/cp-16-2275-2020

Su, H., & Neelin, J. D. (2005). Dynamical mechanisms for African monsoon changes during the mid-Holocene. *Journal of Geophysical Research*, *110*(D19). https://doi.org/10.1029/2005JD005806

Sultan, B., Baron, C., Dingkuhn, M., Sarr, B., & Janicot, S. (2005). Agricultural impacts of large-scale variability of the West African monsoon. *Agricultural and Forest Meteorology*, *128*(1), 93–110. https://doi.org/10.1016/j.agrformet.2004.08.005

Sultan, B., & Janicot, S. (2003). The West African monsoon dynamics. Part II: The "preonset" and "onset" of the summer monsoon. *Journal of Climate*, *16*(21), 3407–3427.

Sultan, B., Janicot, S., & Diedhiou, A. (2003). The West African monsoon dynamics. Part I: Documentation of intraseasonal variability. *Journal of Climate*, *16*(21), 3389–3406.

Swann, A. L. S., Fung, I. Y., Liu, Y., & Chiang, J. C. H. (2014). Remote vegetation feedbacks and the mid-Holocene Green Sahara. *Journal of Climate*, *27*(13), 4857–4870. https://doi.org/10.1175/JCLI-D-13-00690.1

Sylla, M. B., Nikiema, P. M., Gibba, P., Kebe, I., & Klutse, N. A. B. (2016). Climate change over West Africa: Recent trends and future projections. In J. A. Yaro & J. Hesselberg (Eds.), *Adaptation to climate change and variability in rural West Africa* (pp. 25–40). Springer International Publishing. https://doi.org/10.1007/978-3-319-31499-0_3

Tan, L., Cai, Y., Cheng, H., An, Z., & Edwards, R. L. (2009). Summer monsoon precipitation variations in central China over the past 750 years derived from a high-resolution absolute-dated stalagmite. *Palaeogeography, Palaeoclimatology, Palaeoecology*, *280*(3), 432–439. https://doi.org/10.1016/j.palaeo.2009.06.030

Tan, L., Cai, Y., Cheng, H., Edwards, L. R., Lan, J., Zhang, H., et al. (2018). High resolution monsoon precipitation changes on southeastern Tibetan Plateau over the past 2300 years. *Quaternary Science Reviews*, *195*, 122–132. https://doi.org/10.1016/j.quascirev.2018.07.021

Texier, D., Noblet, N., & Braconnot, P. (2000). Sensitivity of the African and Asian monsoons to mid-Holocene insolation and data-inferred surface changes. *Journal of Climate*, *13*(1), 164–181. https://doi.org/10.1175/1520-0442(2000)013<0164:SOTAAA>2.0.CO;2

Thompson, A. J., Skinner, C. B., Poulsen, C. J., & Zhu, J. (2019). Modulation of mid-Holocene African rainfall by dust aerosol direct and indirect effects. *Geophysical Research Letters*, *46*(7), 3917–3926. https://doi.org/10.1029/2018GL081225

Thompson, A. J., Tabor, C. R., Poulsen, C. J., & Skinner, C. B. (2021). Water isotopic constraints on the enhancement of the mid-Holocene West African monsoon. *Earth and Planetary Science Letters*, *554*, 116677. https://doi.org/10.1016/j.epsl.2020.116677

Thorncroft, C. D., & Blackburn, M. (1999). Maintenance of the African easterly jet. *Quarterly Journal of the Royal Meteorological Society*, *125*(555), 763–786. https://doi.org/10.1002/qj.49712555502

Tierney, J. E., Pausata, F. S. R., & deMenocal, P. B. (2017). Rainfall regimes of the Green Sahara. *Science Advances*, *3*(1), e1601503. https://doi.org/10.1126/sciadv.1601503

Tindall, J. C., Haywood, A. M., Salzmann, U., Dolan, A. M., & Fletcher, T. (2022). The warm winter paradox in the Pliocene northern high latitudes. *Climate of the Past*, *18*(6), 1385–1405. https://doi.org/10.5194/cp-18-1385-2022

Tompkins, A. M. (2002). A prognostic parameterization for the subgrid-scale variability of water vapor and clouds in large-scale models and its use to diagnose cloud cover. *Journal of the Atmospheric Sciences*, *59*(12), 1917–1942. https://doi.org/10.1175/1520-0469(2002)059<1917:APPFTS>2.0.CO;2

Wang, Y., Notaro, M., Liu, Z., Gallimore, R., Levis, S., & Kutzbach, J. E. (2008). Detecting vegetation-precipitation feedbacks in mid-Holocene North Africa from two climate models. *Climate of the Past*, *4*(1), 59–67. https://doi.org/10.5194/cp-4-59-2008

Wang, Y. J., Cheng, H., Edwards, R. L., An, Z. S., Wu, J. Y., Shen, C.-C., & Dorale, J. A. (2001). A high-resolution absolute-dated late pleistocene monsoon record from Hulu Cave, China. *Science*, *294*(5550), 2345–2348. https://doi.org/10.1126/science.1064618

Wei, W., & Lohmann, G. (2012). Simulated Atlantic multidecadal oscillation during the Holocene. *Journal of Climate*, *25*(20), 6989–7002. https://doi.org/10.1175/JCLI-D-11-00667.1

Weldeab, S., Frank, M., Stichel, T., Haley, B., & Sangen, M. (2011). Spatio-temporal evolution of the West African monsoon during the last deglaciation. *Geophysical Research Letters*, *38*(13). https://doi.org/10.1029/2011GL047805

Werner, M., Jouzel, J., Masson-Delmotte, V., & Lohmann, G. (2018). Reconciling glacial Antarctic water stable isotopes with ice sheet topography and the isotopic paleothermometer. *Nature Communications*, *9*(1), 3537. https://doi.org/10.1038/s41467-018-05430-y

Werner, M., Langebroek, P. M., Carlsen, T., Herold, M., & Lohmann, G. (2011). Stable water isotopes in the ECHAM5 general circulation model: Toward high-resolution isotope modeling on a global scale. *Journal of Geophysical Research*, *116*(D15), D15109. https://doi.org/10.1029/2011JD015681

Werner, M., Mikolajewicz, U., Heimann, M., & Hoffmann, G. (2000). Borehole versus isotope temperatures on Greenland: Seasonality does matter. *Geophysical Research Letters*, *27*(5), 723–726. https://doi.org/10.1029/1999GL006075

Wu, H., Guiot, J., Brewer, S., & Guo, Z. (2007). Climatic changes in Eurasia and Africa at the last glacial maximum and mid-Holocene: Reconstruction from pollen data using inverse vegetation modelling. *Climate Dynamics*, *29*(2), 211–229. https://doi.org/10.1007/s00382-007-0231-3

Wu, M.-L. C., Reale, O., Schubert, S. D., Suarez, M. J., Koster, R. D., & Pegion, P. J. (2009). African easterly jet: Structure and maintenance. *Journal of Climate*, *22*(17), 4459–4480. https://doi.org/10.1175/2009JCLI2584.1

Xu, X., Werner, M., Butzin, M., & Lohmann, G. (2012). Water isotope variations in the global ocean model MPI-OM. *Geoscientific Model Development*, *5*(3), 809–818. https://doi.org/10.5194/gmd-5-809-2012

Yan, Q., Wei, T., Korty, R. L., Kossin, J. P., Zhang, Z., & Wang, H. (2016). Enhanced intensity of global tropical cyclones during the mid-Pliocene warm period. *Proceedings of the National Academy of Sciences*, *113*(46), 12963–12967. https://doi.org/10.1073/pnas.1608950113

Yang, G.-Y., Methven, J., Woolnough, S., Hodges, K., & Hoskins, B. (2018). Linking African easterly wave activity with equatorial waves and the influence of Rossby waves from the southern hemisphere. *Journal of the Atmospheric Sciences*, *75*(6), 1783–1809. https://doi.org/10.1175/JAS-D-17-0184.1

Yoshimori, M., Yokohata, T., & Abe-Ouchi, A. (2009). A comparison of climate feedback strength between CO2 doubling and LGM experiments. *Journal of Climate*, *22*(12), 3374–3395. https://doi.org/10.1175/2009JCLI2801.1

Zhang, H., Ait Brahim, Y., Li, H., Zhao, J., Kathayat, G., Tian, Y., et al. (2019). The Asian summer monsoon: Teleconnections and forcing mechanisms—A review from Chinese speleothem δ18O records. *Quaternary*, *2*(3), 26. https://doi.org/10.3390/quat2030026

Zhang, R., Yan, Q., Zhang, Z. S., Jiang, D., Otto-Bliesner, B. L., Haywood, A. M., et al. (2013). Mid-pliocene East Asian monsoon climate simulated in the PlioMIP. *Climate of the Past*, *9*(5), 2085–2099. https://doi.org/10.5194/cp-9-2085-2013

Zhang, R., Zhang, Z., Jiang, D., Yan, Q., Zhou, X., & Cheng, Z. (2016). Strengthened African summer monsoon in the mid-Piacenzian. *Advances in Atmospheric Sciences*, *33*(9), 1061–1070. https://doi.org/10.1007/s00376-016-5215-y

Zhang, Z., Li, X., Guo, C., Otterå, O. H., Nisancioglu, K. H., Tan, N., et al. (2021). Mid-Pliocene Atlantic meridional overturning circulation simulated in PlioMIP2. *Climate of the Past*, *17*(1), 529–543. https://doi.org/10.5194/cp-17-529-2021

Zhao, A., Ryder, C. L., & Wilcox, L. J. (2022). How well do the CMIP6 models simulate dust aerosols? *Atmospheric Chemistry and Physics*, *22*(3), 2095–2119. https://doi.org/10.5194/acp-22-2095-2022

Zhao, Y., Braconnot, P., Marti, O., Harrison, S. P., Hewitt, C., Kitoh, A., et al. (2005). A multi-model analysis of the role of the ocean on the African and Indian monsoon during the mid-Holocene. *Climate Dynamics*, *25*(7), 777–800. https://doi.org/10.1007/s00382-005-0075-7

Zhao, Y., & Harrison, S. P. (2012). Mid-Holocene monsoons: A multi-model analysis of the inter-hemispheric differences in the responses to orbital forcing and ocean feedbacks. *Climate Dynamics*, *39*(6), 1457–1487. https://doi.org/10.1007/s00382-011-1193-z

Zheng, W., & Braconnot, P. (2013). Characterization of model spread in PMIP2 mid-Holocene simulations of the African monsoon. *Journal of Climate*, *26*(4), 1192–1210. https://doi.org/10.1175/JCLI-D-12-00071.1

Zhu, J., Otto-Bliesner, B. L., Brady, E. C., Poulsen, C. J., Tierney, J. E., Lofverstrom, M., & DiNezio, P. (2021). Assessment of equilibrium climate sensitivity of the Community Earth System Model version 2 through simulation of the Last Glacial Maximum. *Geophysical Research Letters*, *48*(3), e2020GL091220. https://doi.org/10.1029/2020GL091220